



HAL
open science

Deposition and erosion of a Light-Toned Yardang-forming unit of Mt Sharp, Gale crater, Mars

G. Dromart, Laetitia Le Deit, W. Rapin, O. Gasnault, S. Le Mouélic, C. Quantin-Nataf, N. Mangold, D. Rubin, J. Lasue, S. Maurice, et al.

► **To cite this version:**

G. Dromart, Laetitia Le Deit, W. Rapin, O. Gasnault, S. Le Mouélic, et al.. Deposition and erosion of a Light-Toned Yardang-forming unit of Mt Sharp, Gale crater, Mars. *Earth and Planetary Science Letters*, 2021, 554, pp.116681. 10.1016/j.epsl.2020.116681 . hal-03091803

HAL Id: hal-03091803

<https://hal.science/hal-03091803v1>

Submitted on 22 Nov 2021

HAL is a multi-disciplinary open access archive for the deposit and dissemination of scientific research documents, whether they are published or not. The documents may come from teaching and research institutions in France or abroad, or from public or private research centers.

L'archive ouverte pluridisciplinaire **HAL**, est destinée au dépôt et à la diffusion de documents scientifiques de niveau recherche, publiés ou non, émanant des établissements d'enseignement et de recherche français ou étrangers, des laboratoires publics ou privés.

Deposition and Erosion of a Light-Toned Yardang-forming Unit of Mt Sharp, Gale Crater, Mars

G. Dromart¹, L. Le Deit², W. Rapin³, O. Gasnault⁴, S. Le Mouélic², C. Quantin-Nataf⁵, N. Mangold², D. Rubin⁶, J. Lasue⁴, S. Maurice⁴, H.E. Newsom⁷, P. Pinet⁴, L. Scuderi⁸, R.C. Wiens⁹.

Highlights:

- Using the novel “long distance” capability of the Remote Micro Imager of ChemCam
- Amalgamated eolian deposits compose the Light-Toned Yardang Unit of Mt Sharp
- Exposed yardang forms of Mt Sharp are paleo geomorphic features
- A likely global climate change at the Early-Late Hesperian Transition on Mars
- Exhumed yardangs are relevant supports to study paleo-climatic conditions on Mars

1 **Deposition and Erosion of a Light-Toned Yardang-forming Unit of Mt Sharp, Gale Crater, Mars**

2

3 G. Dromart¹, L. Le Deit², W. Rapin³, O. Gasnault⁴, S. Le Mouélic², C. Quantin-Nataf⁵, N. Mangold², D.

4 Rubin⁶, J. Lasue⁴, S. Maurice⁴, H.E. Newsom⁷, P. Pinet⁴, L. Scuderi⁸, R.C. Wiens⁹.

5

6 ¹Univ Lyon, ENSL, Univ Lyon 1, CNRS, LGL-TPE, 69364 Lyon, France

7 ²Univ Nantes, CNRS, LPG, 44322 Nantes, France

8 ³California Institute of Technology, GPS, Pasadena, California, CA 91125, USA

9 ⁴Univ Toulouse, CNRS, CNES, IRAP, 31400 Toulouse, France

10 ⁵Univ Lyon, Univ Lyon 1, ENSL, CNRS, LGL-TPE, 69622 Villeurbanne, France

11 ⁶University of California Santa Cruz, Earth and Planetary Sciences, Santa Cruz, CA 95064, USA

12 ⁷University of New Mexico, Institute of Meteoritics, Albuquerque, NM 87131, USA

13 ⁸University of New Mexico, Department of Earth & Planetary Sciences, Albuquerque, NM 87131, USA

14 ⁹Los Alamos National Laboratory, Los Alamos, NM 87544, USA

15 **Abstract.** Gale crater is a large impact crater with a ca 5 km thick sequence of stratified rocks in it,
16 expressed today as a central eroded mound (i.e., Aeolis Mons informally named Mt. Sharp). A goal of
17 the current Mars Science Laboratory mission in Gale crater is to investigate the processes that deposited,
18 lithified, and eroded this fill. The Light-Toned Yardang Unit (LTYu) unit, the subject of the present
19 research, is one of the geological units of Mt Sharp. Our specific purpose here is to refine and interpret
20 the imaging documentation of the morphologic and stratal components of the LTYu, at large outcrop
21 scale. In combination with established orbital images, we use the *Remote Micro-Imager* (RMI) of
22 *ChemCam*, a remote sensing instrument currently operated onboard *Curiosity* rover, which provides
23 several types of context imaging. RMI capabilities now include “Long Distance” acquisitions of targets
24 several kilometers away. In these new acquisitions, substantial differences are visible in LTYu yardang
25 attitudes from lowest to uppermost elevations allowing tentative subdivision of the LTYu into subunits.
26 Bedding geometries in the lower LTYu are consistent with eolian dune foresets which collectively
27 prograde towards an average N134° direction. Based on stratal architectures, the LTYu is viewed as an
28 amalgamated stack of at least two, and possibly four, ancient erg systems bounded by large deflationary
29 "supersurfaces". Observations point to a multistory generation of yardangs interpreted to have been
30 successively buried during the stratigraphic building of Mt Sharp. We conclude that the successive
31 sequences of eolian deposition-erosion recorded by the LTYu have been generated by cyclic changes
32 from semi-arid to arid conditions, coupled in climatic cycles, including wind regime change. The
33 regional unconformity that tops the Lower mound formation of Mt Sharp, and the subsequent
34 emplacement of the LTYu, collectively express a clear tendency toward sustained arid environments for
35 this region of Mars around the Early – Late Hesperian transition. Given the large time scale involved
36 (i.e., a few tens of million years as a minimum), we consider it likely that the local evidence for increased
37 aridity in the Mt Sharp stratigraphy is a manifestation of climate change affecting the whole planet.

38 **Keywords.** Mars Climate, Gale Crater, Yardang, Stratigraphy, Eolian, ChemCam

39 1. Introduction.

40 Gale crater is a member of a broad family of impact craters referred to as “Overfilled” (Grotzinger and
41 Milliken, 2012), namely craters that have thousands of meters of layered fill materials, and whose
42 uppermost parts approach or exceed the elevation of the crater margins. In Gale crater, the sequence of
43 stratified rocks occurs today as an eroded mound (i.e., Aeolis Mons informally named Mt. Sharp). One
44 of the goals of the current Mars Science Laboratory (MSL) in Gale is to investigate the processes that
45 deposited, lithified, and subsequently eroded this fill. Mt Sharp’s origin has been the subject of
46 considerable discussion, with various hypotheses including pyroclastic deposits (e.g., Scott and
47 Chapman, 1995), lacustrine deposits (e.g., Malin and Edgett, 2000), and an eolian origin (Bridges et al.,
48 2010; Kite et al., 2013; Anderson et al., 2018).

49
50 The bright unit exposed on the western flank of Mt Sharp, termed the “Light-Toned Yardang Unit”
51 (LTYu; Anderson & Bell, 2010), is the focus of this study. LTYu, one of the geological units that build
52 up Mount Sharp (Le Deit et al., 2013), lies at the boundary of the Lower and Upper formations of the
53 Gale crater fill. It is unconformable with the Lower formation (Malin and Edgett, 2000; Anderson and
54 Bell, 2010), and is in turn onlapped by the Upper mound formation (Le Deit et al., 2013). LTYu was
55 originally described (Malin and Edgett, 2000) as a massive, light-toned unit, the surface of which is
56 dominated by large, sharply-tapered ridges and intervening furrows. Anderson and Bell (2010), using
57 the Mars Reconnaissance Orbiter (MRO) Context Camera (CTX), reported LTYu as a high albedo,
58 uncratered feature. It was then mapped as unit “ume3” by Thomson et al. (2011) and “Cyu” by Le Deit
59 et al. (2013). Anderson & Bell (2010) concluded that scalloped texture of the yardang-forming material
60 of the LTYu suggests that it is soft enough for eolian erosion to scour shallow pits into the surface. Le
61 Deit et al. (2013) proposed that the LTYu might correspond to airfall sediments and wind-blown sands.

62
63 Our purpose is to refine our understanding of the morphologic and stratal components of Gale crater’s
64 LTYu, at large outcrop scale, to reconstruct paleo- depositional and erosional environments, and to
65 decipher the termination scenario of the aqueous story of Gale crater. We used the RMI (Remote Micro-

66 Imager) of ChemCam in combination with the visible CTX and HiRISE (High Resolution Imaging
67 Science Experiment) data of MRO. The RMI, a remote sensing instrument currently operated onboard
68 Curiosity rover, provides several types of context imaging, newly including “Long Distance”
69 acquisitions of targets several kilometers away. The paper presents the geologic evidence derived from
70 this imagery for a genetic model of multistory deposition – early erosion of the LTYu by winds. The
71 paper discusses the role of water in LTYu deposition/preservation, the timing and duration of LTYu
72 emplacement, and the timing of yardang formation. It closes with remarks about possible atmospheric
73 conditions in Gale crater at the Early -Late Hesperian Transition.

74

75 2. Geological context

76

77 Gale crater, a ca 155 km diameter impact crater, is located near the martian equateur (5°S/138°E; Fig.
78 1), at the planet’s crustal dichotomy. The crater contains a thick, ca 5 km, sequence of stratified rocks
79 that make up the central mound, the maximum elevation of which is similar to that of the southern crater
80 rim but which is several kilometers higher than the degraded northern rim (Fig. 1A). Based on crater
81 distributions on the Gale ejecta blanket, Gale crater formed 3.7 ± 0.1 Ga ago (Thomson et al., 2011; Le
82 Deit et al., 2013) at the Noachian-Hesperian transition. The early degradation of the crater rim supplied
83 sediments which prograded away from the rim, aggrading an episodically filled lake basin (Grotzinger
84 et al., 2015). This lake system likely intermittently existed for thousands to millions of years implying
85 a wet climate. The complete sequence of filling Gale crater and exhumation of Mt Sharp largely
86 happened within a few hundred million years after Gale crater formed (i.e., by the end of Hesperian
87 times) (Thomson et al. (2011).

88

89 Curiosity landed in the northwestern crater floor of Gale crater (Vasavada et al., 2014), and has traversed
90 >7 km to reach the lower units of Mt. Sharp. The dark-toned, nearly flat-lying layers of the lower units
91 yield orbital spectral signatures of phyllosilicates, mono and polyhydrated sulfates, and ferric oxide
92 (hematite) (Milliken et al., 2010; Fraeman et al., 2016). From observations by Curiosity, the thick, ca

93 400 m, sequence of the lower units has been inferred to consist of fluvio-lacustrine deposits (e.g.,
94 Grotzinger et al., 2015).

95

96 Higher on Mt Sharp, well above even the future traverse of Curiosity, the LTY-forming material is a
97 distinctive, high CTX albedo feature well exposed on the northwest flank of the Gale crater mound (Fig.
98 1). From orbit, the LTYu displays a general lens-shape that covers an area of about 70 km². In CTX
99 images, the material appears to be a massive deposit, with a surface that has been eroded into yardang-
100 like forms. Infrared CRISM spectral signatures of LTYu typically are those of the ubiquitous Martian
101 dust with a very weak sulfate signature detected locally (Milliken et al., 2010; Thomson et al., 2011).

102

103 The LTYu lies along a ca 15° slope between -3990 and -1674 m, clearly and unconformably overlying
104 the lower units of Mt Sharp, namely the Syu1 unit (Small yardang unit 1; Le Deit et al., 2013), as
105 demonstrated by a crater partially exhumed from beneath the LTYu (Malin and Edgett, 2000; Fig. 1B).
106 The relationships of the LTYu with the Syu1, and the observation made by Le Deit et al. (2013, fig.
107 13b) that the topmost yardang forms of the LTYu are buried by a set of continuous, planar strata of the
108 Small yardang unit 2 (Syu2) (i.e., lower Upper Mound unit of Anderson and Bell, 2010) supports an
109 interpretation that the LTYu occurs as a stratigraphic unit enclosed in the Upper mound formation, and
110 not as a distinct, more recent formation patched on the flank of a previously eroded central mound.
111 According to Le Deit et al. (2013), the LTYu is a thin stratigraphic unit (i.e., 100 to 200 m) which was
112 emplaced at the Early – Late Hesperian transition.

113

114 The Benched unit (Bu; Fig. 1B), a thick stratigraphic package of Mt Sharp characterized by a more
115 uniform albedo and large-scale cliff-bench style geomorphic expression in some areas, lies above the
116 LTYu and the Syu2 (Anderson et al., 2018).

117

118 3. Data sets and methods

119 3.1. Orbital camera data

120 Orbital visible images were used: to provide the general geological and geomorphological contexts of
121 the LTYu; measure contact geometries of stratigraphic units; measure the morphological aspect of
122 distinct yardang-bearing subunits; delineate the bedding geometry of the deposits and; provide context
123 for Long Distance RMI (LD RMI) views from Curiosity rover.

124

125 We used the basemap generated for science and engineering operations conducted by the MSL Curiosity
126 rover (https://bit.ly/MSL_Basemap). The basemap and associated DTM (Digital Terrain Model) were
127 built from two types of visible images: CTX, for which there is an extensive coverage at 6 m/pixel; and
128 ~0.27 m/pixel data from the HiRISE instrument. Where available, we used ultra-highly resolved HiRISE
129 stereo images derived DTMs (1 m) (Kirk et al., 2008) to measure the geometry of contacts and beds,
130 and to project the ground LD RMI images over the topography.

131 Morphometric attributes of the ridges were measured manually using *Adobe Illustrator*[®] software
132 applied to MOLA (Mars Orbiter Laser Altimeter) DTM elevations. We did not consider the attitudes of
133 all individual ridges and restricted our measurements to larger forms (i.e., length >30 m) because
134 positioning is too uncertain and measurements are too inaccurate for small features. Accordingly, the
135 analysis does not yield the comprehensive distribution of the forms. However, this method, repeatedly
136 applied across the whole LTYu, was sufficient to disclose salient differences between morpho-
137 stratigraphic subunits of the LTYu. To evaluate the accuracy of our method, a second operator repeated
138 measurements on 39 ridges of the lower part of the LTYu. Results show that: (i) average of direction
139 differences was minimal (i.e., 1.95°) between observers but individual differences up to 10° occurred;
140 (ii) the magnitude of the relative errors on measured lengths and widths is $\pm 5\%$.

141

142 *ArcGIS*[®] extension Layer Tools (Kneissl et al., 2010) were used to quantify the geometry of the LTYu
143 basal bounding surface. This tool combines spatial coordinates of measured points from imagery with
144 corresponding elevation values extracted from an underlying DTM. X,Y,Z data from measurements
145 along a geologic contact allow construction of planes describing the extent of the geological surface of
146 interest. The surface is defined in terms of planar dip and dip direction by at least three measurement

147 points. For more than three points, the best-fitting plane is computed using a polynomial fit. Output from
148 tool comprises dip-angle and dip-direction values of the interpolated planes.

149

150 3.2. Ground visible data: Long Distance Remote Micro-Imager (LD RMI) images

151 It is difficult to interpret stratal architectures of a deposit (e.g., bedding geometries and truncations)
152 based purely on the plan view provided by orbital data. Accordingly, we used a ground camera (RMI)
153 which allows cross-sectional views of strata. ChemCam's RMI instrument affords the finest pixel scale
154 on the rover mast with $19.6 \mu\text{rad}/\text{pixel}$ (Le Mouélic et al., 2015). The RMI telescope was originally
155 designed to provide close-in context images for LIBS analyses. After the loss of the Continuous
156 Wavelength Laser function, which focused the RMI telescope, an autofocus procedure was implemented
157 that offers the advantage of being operational at all distances, including imaging of targets up to several
158 kilometers away (Peret et al., 2016; SM_Text 1).

159

160 The smallest features that can be distinguished at the center of these LD RMI images at best focus range
161 between [6 - 10] cm at 1 km. At 5 km the finest resolution [0.3 - 0.5] m is equivalent to HiRISE orbital
162 resolution. Usually a series of individual LD RMI images is acquired with an appropriate offset between
163 images (6 to 12 mrad) which ensures an overlap of the images and the full coverage of the target. The
164 individual images are stitched into mosaics and then subjected to corrections to improve, for example,
165 the image sharpness (SM_Text 1).

166

167 Using the *Visibility Tool* of *ArcMap*®, LD RMI mosaics are projected as view sheds onto the DTMs.
168 The projection ensures the control of projective geometry issues associated with the LD RMI mosaics,
169 and facilitates the calculation of the elevation range of the targets.

170

171 4. Observations

172 4.1. Morphological elements

173 From orbit, much of the light-toned material surface is textured by variably contiguous low ridges and
174 shallow depressions (Fig. 2). These ridges are several tens to a few hundred meters-long, with a large
175 aspect ratio (length/width) $\geq 4:1$ (SM_Table 1). Local relief between crests and troughs ranges from 5
176 to 25-30 meters. However, the pattern of the forms is not homogeneous across the LTYu (Fig. 2). Based
177 on substantial textural differences that appear from the western to eastern exposures (i.e., from the lowest
178 to uppermost elevations) the surface of the LTYu can be tentatively subdivided into four (4) subunits
179 (Fig. 2): Lower LTY; Middle LTY; Upper LTY, and Top LTY.

180 The clearest morphological difference is in between the stepped topography of the lower subunit ridges,
181 and the variably elongated, lens-shaped pattern of the morphologies of the upper subunits. The lower
182 stepped pattern results from the intersection of three straight ridge crest directions. It yields distinct
183 dissected alignments of triangular facets in plan view, with a smooth, gently sloping flank, and a steep,
184 cliff-forming side (i.e., transversally asymmetric profiles) (Figs 2B, 4A). Cross-sectional RMI views
185 show that the Lower LYTu is made up of a stack of ~10 m-thick, light-toned, resistant, clearly-dipping
186 (i.e., apparent dip up to 12°SW) elongated forms (i.e., ridges) separated by recessive horizons (Fig. 4C).

187 The upper subunits display forms that can be distinguished according to the number and distribution of
188 the long-axis direction of the ridges (Fig. 2; SM_Table 1), and from geometric characteristics of the
189 forms observed in plan view (Fig. 2C, D, E). Forms of the Middle LTY subunit show teardrop-like
190 morphologies with blunt heads and convex, broad tapered tails. The forms of the Upper LTY subunit
191 are rhomboidal in shape and exhibit variably flattened crests lines. It is difficult to separate individual
192 forms from each other in the Upper LTY subunit because the larger forms are themselves dissected into
193 "self-similar" smaller forms, giving way to a quasi "braided" pattern. The forms of the Top LTY subunit
194 present streamlined ridges with steep and narrow flanks, separated by flat-floored troughs.

195 4.2. Basal unconformity

196 Thomson et al. (2011) determined the attitude of the contact between the LTYu and the surrounding
197 units by identifying intersections between mapped outline of the entire LTYu and topographic profiles
198 from MOLA data. They concluded that the contact is best described by a planar surface with a strike

199 and dip of N45°E, 12.1°_NW (i.e., inclined to the NW). However, the means by which the geometry of
200 the basal surface of the LTYu has been reconstructed cannot be adopted: the bounding surface of the
201 southeastern LTYu is clearly overlain by the Upper mound formation, namely by the Syu2 unit of Le
202 Deit et al. (2013; fig. 13b), and is thus the top surface of the LTYu, and not its basal surface. We here
203 restricted the measurement of the contact attitude to the western part of the LTYu, an area where the
204 unconformable relationship of the LTYu with the underlying unit is clearly exposed. This surface dips
205 to the northwest (N53°-55°E strike direction), with locally variable angles increasing from 6.5° in the
206 southern section of the contact to 15.5° in the northern section (Fig. 3A).

207 Close-ups of HiRISE images that cover the contact show that a paleo-crater has been stripped off and
208 filled prior to the deposition of the LTYu (i.e., partially-exhumed crater of figure 3C). As well, a series
209 of ridges and troughs forms at the top of the upper Syu1, are buried by the lowermost LTYu deposits
210 (Fig. 3B).

211 4.3. Stratal components of the Lower LTYu

212 Stratal architectures were analyzed for the lower LTY subunit only, for which we have both the RMI
213 and HiRISE images that can advantageously be combined (Fig. 4). Ground and orbital imagery (Fig. 5
214 & 6) reveal well-exposed, and extensive straight bed traces. Cross-sectional views reveal that the
215 resistant ridges are internally composed of sets of gently dipping to sub-horizontal, mostly planar, evenly
216 stacked individual beds (Fig. 5). Only a few examples of erosional stratigraphic surfaces intersecting
217 the modern slope have been identified (i.e., local surfaces that bound bed sets apparently truncating
218 other bed sets). Orbital plan views (Fig. 6) show bed traces running approximately parallel with apparent
219 uniform spacing. These traces have a linear to curvilinear pattern that suggests prevalent planar
220 geometry for the beds. Collectively, figures 5 & 6 reveal that the beds are arranged as shingled
221 prograding clinobeds. The strike azimuth of the bed traces in plan view is fairly steady, around the
222 average direction of N44°. It can thus be inferred that the clinobeds dip towards the southeast, which
223 would be the dominant direction of the net sediment transport.

224

225 5. A model: Multistory deposition-erosion by winds

226 5.1. Deposition/preservation of the Lower LTY subunit

227 In the Lower LTYu-composing material, observed dips, and the very finely- and evenly-bedding
228 geometries are interpreted as strike sections of individual strata (Fig. 5) that collectively prograde
229 towards a N134° direction (Fig. 6). The large lateral extension and planarity of these now-variably-
230 eroded dipping beds, together with low variation in bed dip azimuths in orbital imagery (Fig. 6)
231 collectively are **consistent with** eolian dune foresets. Moreover, the fact that some resistant beds are
232 uniformly spaced (i.e., alternating with recessive interbeds), at the toe of the ridge-form in particular,
233 points to cyclic bed deposition, which is a characteristic feature of eolian tracts. Conversely, counter
234 dipping beds that would point to the development of antidune systems, typical of pyroclastic flow
235 deposits, or extensive draping ashfall beds have not been observed.

236
237 The unscaled, two-dimensional model we propose for deposition and preservation of the bed sets of the
238 Lower LTY subunit (Fig. 7) is derived from the application to our observations of the theoretical model
239 of Kocurek (1986). The theoretical diagram (SM_Fig.1A) describes the generation of sets of cross-strata
240 by migrating and climbing eolian dunes. These cross-strata sets are bounded by surfaces referred to as
241 first-order surfaces. The theoretical model is derived from a wealth of examples available in the
242 terrestrial stratigraphic record (e.g., the Jurassic Navajo Sandstones in Zion National Park; SM_Fig.1B).

243
244 By extension, it is speculated that the model of net deposition for the Lower LTY subunit applies to the
245 entire LTYu. The main strength for the LTYu model as a multistory deposition-deflation by wind, lies
246 in the fact it assimilates all of the observations we have, which derive from a synergetic analysis of well-
247 resolved orbital and ground data. Conversely, a potential weakness of the model is that it is also
248 supported by negative evidence, namely observations that do not fit alternative interpretation such as
249 tephra, or fluvial deposition.

250

251 There is some inadequacy of directly supporting observables for wind interpretation, and a definite point
252 of weakness lies in the limitation in the number and quality of appropriate observables, namely: (i) the
253 dataset is not homogeneous across the object of analysis (i.e., LD RMI and HiRISE stereo DEM's are
254 only available for the Lower LTY subunit), so the fine stratal organization of the upper LTY subunits
255 cannot be determined; (ii) our dataset derives from remote analysis and sorely lacks small scale in-situ
256 outcrop observation. For example, documentation of the development of several superimposed orders
257 of stratification and cyclicity (uniform vertical spacing of beds and first-order bounding surfaces), which
258 is typical and diagnostic of eolian deposits, cannot be really achieved and is only suspected here.
259 Likewise, even if our model predicts accumulation in dry eolian systems because of the apparent absence
260 of interdune elements, we cannot rule out wet interdunes from the RMI images alone, because a lot of
261 eolian sandstones have indications of wet interdunes only when viewed from a few meters away (e.g.,
262 crinkly laminae formed by alternating wetting and drying and/or precipitation and dissolution of
263 evaporites within lowermost foresets or in the strata immediately underlying the bounding surfaces;
264 Irmen & Vondra, 2000). Another aspect of the lack of control at the small outcrop scale is that we are
265 unable to confirm the model-predicted occurrences of uniformly -spaced, quasi-planar, ramping-up
266 truncation surfaces (i.e., first-order surfaces; SM_Fig. 1) within the Lower LTYu. This may be due to
267 the propensity the first-order bounding surfaces have to lie in recessive intervals, and so are often
268 covered by scree.

269

270 5.2. Stratigraphic geometries of the upper LTY subunits

271

272 As for the upper LTY subunits as a whole, we propose a geometric model for the net deposits (Fig. 8A).
273 The graphic model is a stratigraphic cross-section derived from the orbital plan views. The four (4)
274 LTYu subunits that have been distinguished from the attitudes of the morphological elements (Fig. 2)
275 are parallel bands that intersect the general slope of the LTYu. We believe that these morphological
276 units express stratigraphic entities separated by discontinuities. Supporting evidence for this
277 interpretation comes from the fact that the lines that bound the LTY subunits appear to run roughly
278 parallel with the basal unconformity (SM_Fig.2). Conversely, a weakness of this model arises from the

279 fact that the contacts between the LTY stratigraphic subunits, referred to as sub-unconformities, appear
280 from orbit as amorphous features and generally, with probable exception of the contact between the
281 Lower LTY and the Middle LTY subunits (SM_Fig. 3), cannot not clearly be delineated. The poor
282 delineation of the contacts may come from non-optimal HiRISE camera angles, weak low rock tonality
283 contrasts, or possibly because these contact surfaces are paraconformities (i.e., similar bedding attitude
284 on both sides of the discontinuity).

285 Interpretation of wind-influenced control of internal sub-unconformities of the LTYu is derived from
286 two observations. First, the characteristics of the major basal contact geometry (i.e., truncation of
287 underlying strata, declivity between 6-15°, minimal elevation difference of about 1 km) collectively are
288 inconsistent with a simple subaqueous depositional process and fits well with eolian control of the
289 erosional surface. Second, sub-unconformities that bound LTY stratigraphic subunits are parallel with
290 the basal unconformity, a feature consistent with large eolian deflationary surfaces.

291 There are wealth of analogs in the eolian terrestrial record of stratigraphic organizations similar to those
292 depicted here for the LTYu. The bounding surfaces of the LTYu (i.e., internal sub-unconformities of the
293 LTYu) show a minimal extension of several kilometers with separate packages of LTY material of 100-
294 300 meters in thickness (Fig. 8A). A gross terrestrial analog for these surfaces is available in Western
295 USA basins where, in some localities, Paleozoic and Mesozoic vertical stacks of eolian genetic
296 sequences are bounded by extensive (tens of kilometers) surfaces that are relatively flat, and at angular
297 discordance with the first-order surfaces. These large, regional surfaces have been called "super
298 bounding surfaces" (Kocurek, 1988) or "supersurfaces" (Brookfield, 1992). An excellent example is the
299 succession observed in southern Utah where the stratigraphic column in order shows a sequence of:
300 Navajo Sandstone (100 - 600 m) - J1 Unconformity - Temple Cap Sandstone (50 - 100 m) - J2
301 Unconformity - Page Sandstone (20 - 60 m) (Blakey et al., 1988; 1996). The major unconformity
302 underlying the LTYu and sub-unconformities within the LTYu collectively are herein interpreted to be
303 super bounding surfaces, even though their geometry is not horizontal and their areal development is
304 apparently much more limited than that found in the Earth basin referred to here. We think these
305 differences are due to the unique position of the eolian LTYu system on the flank of a paleo-mound.

306

307 5.3. Yardang formation

308

309 Yardangs are spectacular erosional landforms found in major terrestrial deserts globally. They often
310 occur as great fields up to a few tens of millions of km² in extent (e.g., McCauley et al., 1977). Satellite
311 imagery analysis coupled with field studies show yardangs to be relatively straight, elongate,
312 asymmetric spurs sculpted upon variably lithified and aged material (e.g., El-Baz et al., 1979; Wang et
313 al., 2018). Numerous recent surveys have addressed terrestrial yardang forms (e.g., Laity, 2011; Zhao
314 et al., 2018). The consensus is that the prerequisites for yardang development are strong, unidirectional
315 or reversing winds in arid regions over barren continuous rock exposures or over the surfaces of poorly
316 consolidated sediment. The studies have found that the long, shallow troughs separating yardangs are
317 locations where most of erosion takes place. On Mars, yardangs were observed in the earliest orbiter's
318 images (e.g., McCauley, 1973; Ward, 1979) with these forms typically occurring in equatorial regions,
319 including in particular the extensive Medusae Fossae Formation (MFF), east of Tharsis (e.g., Mandt et
320 al., 2008).

321

322 Surface elements of the Gale central mound LTYu are interpreted as yardangs because of the
323 morphological similarity they share with the terrestrial yardangs (e.g., teardrop-like morphologies of the
324 Middle LTY subunit closely fit the *whaleback* type yardangs defined by Wang et al., 2018). The shape
325 of these troughs by wind is very likely and alternative formation processes (gravity-driven erosion
326 by mass and fluvial flows) are precluded because: (i) the overall direction of the modern slope is toward
327 the NW, in distinct contrast to the primary direction of erosional features that run parallel to the main
328 yardang's axes (Fig. 2; SM_Table 1); and (ii) valleys in between the yardangs crests appear not to be
329 fan-terminated downslope.

330

331 We hypothesize that the LTYu yardang's ultimate morphology results from the dual influence between
332 the original bedding geometries and the primary direction of the erosive winds. Supporting evidence

333 comes from the southern part of the Lower LTYu where bedding planes dip southeast (N134°; Fig. 6)
334 and appear to control yardang transversal asymmetry: the smooth, gentle faces of the individual
335 yardangs fit bed dips whereas the steep faces represent bed strike sections. Elongations of the yardangs
336 crests were in turn likely generated by superimposed, westerly winds blowing in N67° and N83°
337 directions (Fig. 4A). HiRISE images that cover the transversally-symmetrical yardang forms of the
338 upper LTY subunits (Fig. 2C, D, E) suggest subhorizontal, more gently dipping internal bounding
339 surfaces, such as expressed in our cross-section (Fig. 8A).

340

341 Beyond the morphology of the yardang shapes, there are clear differences in how the units have
342 weathered. The lower and middle units appear as cliff -forming units suggesting a substrate prone to
343 fractures (Fig. 2). The upper units show less of this type of failure with many yardangs tailing off rather
344 than failing in abrupt cliffs. This difference could be reflective of distinct degrees of induration of the
345 material prior to weathering.

346 Our model for the yardang formation is that the general elongation of the yardang forms is controlled
347 by the prevailing erosive wind direction whereas the transversal profiles of the individual forms are
348 influenced by the internal bedding geometry and, possibly, by the degree of induration of the deposits.
349 This model implies that the Lower LTY subunit - latitudinal dominant direction, and the upper LTY
350 subunits group - meridian dominant direction, must have been shaped by very distinct wind regimes.

351 To summarize, the stratigraphic LTYu of Mt Sharp is viewed, based on the analysis of the stratal
352 architectures, to be an amalgamated stack of at least two, possibly four, ancient erg systems. From the
353 analysis of the surface textures, the morphological elements are inferred to be yardangs (i.e., forms been
354 generated by wind erosion). The duration estimated for the deposition of the LTYu including the
355 generation of the basal unconformity, the timing of the yardang formation, and the possible source of
356 the yarding-forming material are discussed below.

357 6. Discussion

358 6.1. The role of water in the deposition/preservation of the LTYu

359

360 The purpose of the following discussion is to assess the potential influence of regional moisture in the
361 accumulation and preservation of the LTYu's ergs.

362

363 There is no direct evidence of the influence of surface or subsurface water on the accumulation of the
364 eolian material of the LTYu. This does not mean there was not, because as noted above, potential
365 indications of wet interdunes might be too subtle to be seen in available imagery. Conversely, we note
366 that the presence of free surface water, or water as capillary fringe in the subsurface, is not a limiting
367 condition for erg deposits to accumulate. Marzolf (1988) acknowledged that a well-drained, low-relief
368 surface is an important enhancing factor for erg development, and that fluvial processes only lead to
369 significant concentration of sand that is subsequently deflated into erg dunes. On Mars, one could expect
370 that total sediment yield increase monotonically with surface runoff, because there is no moisture-
371 related, vegetation cover to reduce runoff. Additionally excessive runoff reduces the ability for wind to
372 deflate the surface due to sand stabilization by water saturation in the initial sand accumulation.
373 Conversely, a prolonged arid period where fresh alluvium is not generated, could favor formation of
374 desert pavement, which limits surface wind deflation (Marzolf, 1988).

375 Additional indirect information about the presence of water comes from the preservation itself of erg
376 deposits between the sub-unconformities (i.e., supersurfaces). The thickness of the deposits left by an
377 erg in the rock record is both a function of deposition and subsequent removal of these deposits during
378 supersurface formation. The extent of erg-sediment removal during supersurface development is
379 governed by: (1) deflation to the water table; (2) deflation to a point where a protective armored lag
380 occurs; (3) development of a protective mantle of vegetation; or (4) the time interval before deposition
381 by ergs or other depositional systems (e.g., alluvial fan) resumes (Kocurek, 1988). These reasons are
382 not mutually exclusive. With respect to our study, points 1) and 2) are sound possibilities but certainly
383 not unique processes since the supersurfaces of the LTYu are not planar and horizontal (Fig. 8A). Point
384 4 is related to the migration of sand seas by changing wind patterns due to changes in the arrangement
385 of the Wilson's nodes (Wilson, 1971). In ergs, sand is deflated from and/or transported across areas of

386 accelerating or diverging winds, areas referred to as "node of attachment", to accumulate in areas of
387 converging and/or decelerating flow, referred to as "nodes of separation". We consider point 4 to be the
388 most likely in that: (i) the LTYu itself is overlain by the Benched unit, another erg system (Anderson et
389 al., 2018); (ii) LTYu sub-unconformities have an apparent limited lateral extent and are intersecting
390 each other (Fig. 8A).

391

392 The development and the preservation of erg deposits of the LTYu point to the existence of a temporally
393 equivalent and geographically adjacent alluvial system where fluvial deposits were deflated to provide
394 a source of particles that were entrained to form eolian dunes, and from which water table high stands
395 driving preservation of eolian deposits might have been sustained. Considering the observed dominant
396 paleo sand transport direction towards the center of Gale crater (Fig. 6), an intuitive location for the
397 alluvial system development would be the interior flank of the NW crater rim. The stratigraphic
398 elevation range of the LTYu that is ca -3.3 to -1.9 km is consistent with the modern northern rim
399 elevation of -2.46 km (Irwin et al., 2005) given the facts that the northern rim originally may have been
400 slightly higher and that we have observed that eolian deposits are composed of bedforms climbing up
401 the central mound.

402

403 If we admit the existence of an alluvial system that was deflated to feed eolian dunes, we are still left
404 with the question of the ultimate source of this material. The geographic proximity, the similarity of the
405 bright tone, and the textural comparison of the LTYu with the MFF have led some authors (e.g.,
406 Zimbelman & Griffin, 2010; Tanaka et al., 2014) to consider the LTYu as an isolated remnant of the
407 regional widespread MFF. While the primary depositional mechanism(s) of the MFF remains uncertain,
408 volcanic airfall, ignimbrites, or eolian dust are leading hypotheses (e.g., Mandt et al., 2008). Whatever
409 its origin, it is clear that intermittent (Di Pietro et al., 2018) and subsequent (Burr et al., 2009) reworkings
410 by fluvial systems of the MFF primary deposits have occurred. The final view that the eolian systems
411 of the LTYu are recycled deposits of the MFF is consistent with the recent findings that a significant
412 part of the MFF may have been deposited during the Hesperian (Kerber & Head, 2010; Zimbelman &
413 Scheidt, 2012).

414

415 6.2. Timing and duration of the LTYu deposition

416 The LTYu marks the resumption of sediment accumulation above a major hiatal stratigraphic contact
417 that is the basal unconformity. The presence of an exhumed crater (Fig. 3C) and paleo-yardang forms
418 buried by the basal LTYu deposits indicate that the underlying dark-toned layers of the Syu1 became
419 lithified enough to retain craters and be partially eroded before the lighter unit deposition. While a
420 consolidation of sediments entails a certain period, the question is how much time actually is collapsed
421 within this contact?

422 The partly exhumed crater currently is a poorly rounded, very shallow pit ~600 meters in diameter and
423 a few meters deep (Fig. 3C). It is a fairly planar feature which does not show a real rim, suggesting it
424 has been planed off prior to the LTYu deposition. A power law (Garvin et al., 2003) between the martian
425 crater depths and diameters predicts this crater must have had an initial depth ranging in between 10 and
426 20 meters, so that it can be inferred that its rim has been eroded by a few tens of meters. Using crater
427 obliteration rates of about 1 m/My for the Hesperian - Amazonian (Quantin-Nataf et al., 2019), the aerial
428 exposure time of the crater retention surface, after impact, must have been in the range of one to a few
429 tens of million years.

430 An another way of evaluating how long the top surface of the Syu1 has been exposed is to calculate the
431 lapse-time required for the surface to have a significant chance of having been impacted, at the Early-
432 Late Hesperian age (i.e. 3.4 Gy) by a bolide able to generate a 600 m wide crater. The calculation is
433 based on the crater size frequency distribution from Hartmann (2005) and the crater production function
434 from Neukum et al. (2001). If we take as a boundary condition that the exposed surface was about 2,000
435 km² (assessed original extent of the exposed surface), 70 km² (current extent of the LTYu), 14 km²
436 (current extent of the visible contact surface), the computed recurrences times are about 14, 400, and
437 2,000 Myrs, respectively. This tentative calculation that yields a range of over two orders of magnitude
438 is not very relevant by itself. It only shows that it is consistent with the above inference of an aerial
439 exposure duration of at least few tens of million years.

440 As to how long the net accumulation of the entire exposed LTYu itself took, it can be approximated as
441 several tens of million years, based on the terrestrial analog from southern Utah. According to Blakey
442 et al. (1996), the major stratigraphic erg system in this region enclosing two deflationary supersurfaces
443 initiated in the Early Jurassic and terminated in the Middle Jurassic, spanning a time interval of about
444 20 Myrs. It should be added that a time-interval of 20 M. earth years does not necessarily conflict with
445 a possible control of erosion-deposition cycles by the variation of Mars' orbital parameters. For example,
446 it has been shown for the past 10 M. earth years on Mars that the period of high-mean obliquity is 4
447 Myrs at least (Laskar et al., 2004), so that each LTYu subunit might have been deposited during a period
448 of high obliquity.

449

450 6.3. Timing of the yardang formation

451

452 The apparent lack of craters on the surface of the light-toned yardang-forming material itself may
453 suggest that the development of the yardang forms is quite recent (Anderson & Bell, 2010). However,
454 Le Deit et al. (2013; fig. 13b) have shown that yardang forms of the LTYu are buried by a set of
455 continuous, planar strata of the Syu2. Another argument for an early development of the LTYu yardang
456 forms comes from the observation that the overlying and more recent units (i.e., Syu2 and Bu) do not
457 exhibit yardangs. Similarly, if we accept that the yardang long axes are subparallel to the prevailing
458 wind directions, then it is difficult to reconcile the nearly orthogonal change of the wind prevailing
459 directions between the Lower LTY subunit and the upper LTY subunits (Fig. 2) with deflection of a
460 single dominant wind over such a short spatial scale. Moreover, neither of the two prevailing directions
461 (i.e., East-West and North to South respectively) is consistent with recent, Mt Sharp related, up- or
462 downslope-wind.

463

464 These observations rather suggest that at least two distinct yardang-generating wind episodes occurred
465 during the initial development of Mt Sharp, and not after Mt Sharp formed. Our interpretation for the
466 LTYu is that a package of eolian sand was deposited over an erosional surface of yardangs eroded into
467 the previous package of indurated material. This repeated to form at least two (2), possibly four (4),

468 apparent sequences involving eolian sand deposition, induration to some degree, and erosion to create
469 yardangs. It is thought that the LTYu was deposited, partially lithified, and eroded into yardangs
470 cyclically. The successive burial-related induration of the yardangs have likely made them difficult to
471 obliterate, so that recent degradation must have been respective of their original form. Incomplete
472 lateral burial of the Lower LTY subunit would have caused the superimposition of several yardang
473 directions over it.

474

475 Such a type of deposition-erosion sequence has been documented on Mars in the MFF of the Amazonis
476 Planitia Region (Wells & Zimbelman, 1989; Mandt et al., 2009). In that area, two sets of yardangs were
477 formed by winds of nearly orthogonal directions. An older set of yardangs was buried by a deposit 100
478 m in thickness, and later exposed by the easterly winds that formed the younger yardangs. **Similarly,**
479 **Chojnacki et al. (2020) have reported in Valles Marineris, atop Hesperian-aged layered deposits, a**
480 **lithified field of paleo-barchan dunes that climbed up onto the flanks of an eroded sedimentary mound,**
481 **before being lithified.**

482 Finally, it should be noted that lithified yardang forms apparently exist in the Earth's stratigraphic
483 record. An example comes from the Canyonlands National Park, SE Utah where partly exhumed,
484 aligned sandstone ridges occur at the upper unconformable surface of the Lower Permian (Leonardian),
485 and are onlapped by the Lower Triassic (Tewes & Loope, 1992). The potential time gap that here
486 corresponds to the paleo-yardangs is of the magnitude of 20 Myrs.

487

488 7. Conclusion: Atmospheric conditions in Gale crater in the Late Hesperian

489

490 The eolian material of the LTYu was deposited in a context of regional aridity. However the putative
491 cycles of eolian deposition – and (partial) erosion which compose the LTYu are believed to reflect
492 change in the regional moisture budget, swinging from semi-arid (deposition) to arid (erosion)
493 conditions. Assuming that alluvial fans are the original sources of sands, it is expected that: (i) a
494 decreasing fluvial flow-recurrence interval, as a result of increasing moisture, will increase sand

495 deflation availability and raise erg water table levels, favoring accumulation and preservation of ergs
496 respectively; (ii) conversely, increased aridity will cause a dwindling of sand supplied to ergs and favor
497 development of yardangs and erosional bounding supersurfaces. We have also seen that the generation
498 of bounding supersurfaces might be influenced by the migration of sand seas due to changes in the
499 arrangement of the Wilson's nodes. Given the high probability of quasi-static physiographic conditions
500 in Gale crater, a change of Wilson's nodes implies a regional change of wind regime.

501

502 Our final view is that cyclic aridity changes must have been coupled in climatic cycles with changes in
503 wind regimes to generate the sequences of eolian erosion-deposition recorded by the LTYu. We further
504 propose that the major unconformities (i.e., basal and top LTYu unconformities) have primarily been
505 associated with severe and prolonged aridity whereas sub-unconformities within the LTYu have primary
506 been related to wind regime changes. Whether these putative climatic cycles recorded in Gale crater are
507 global and periodic, and so related to the variations in orbital and spin axis parameters of the planet,
508 cannot be resolved at this time. At any rate, what can be highlighted here is that the regional
509 unconformity that separates the Lower and Upper mound formations of Mt Sharp, and the subsequent
510 emplacement of the LTYu, together express a clear tendency toward more arid environments for that
511 region of Mars around the Early – Late Hesperian transition. Given the large time scale that is involved
512 (i.e., a few tens of million years at least) we consider it likely that the local evidence for increased aridity
513 in the Mt Sharp stratigraphy is part of a climate change affecting the whole planet.

514

515 Acknowledgments

516

517 The authors gratefully acknowledge support from the NASA Mars Science Laboratory Mission and the
518 efforts of the MSL engineering and science operations teams. This work was supported in France by the
519 Centre National des Etudes Spatiales (CNES) and the Centre National de la Recherche Scientifique
520 (CNRS). G. Dromart, L. Le Deit, C. Quantin-Nataf, N. Mangold, and D. Rubin thank Fondation des
521 Treilles for support for a meeting during which they had the opportunity to discuss about eolian
522 sedimentation on Mars. Gratitude is due to R. Anderson, L. Edgar, and K. Herkenhoff (USGS) for

523 discussions that helped improve this work. Thanks to Drs. Kenneth Edgett (Malin Space Center) and
524 Robert Sullivan (Cornell) for their very valuable feedback on an early version of the manuscript, and to
525 anonymous reviewers for their constructive comments.

526

527 **Figure Captions**

528

529 Fig.1: (A) CTX mosaic of Gale crater; Fig1B indicated by light pink box. (B) Inset showing key
530 geological units, including in a stratigraphic ascending order the Small yardang unit 1 (Syu1), Light-
531 Toned Yardang unit (LTYu), Small yardang unit 2 (Syu2), and Benched unit (Bu), and major
532 unconformities that bound these units; white dot is the rover location from which the LD RMI view of
533 (C) was shot, and white dashed bars delineate the field of view of (C). (C) Long-Distance Remote Micro
534 Imager mosaic (ChemCam instrument onboard Curiosity Rover) showing: (i) the strong rock tone
535 contrast between the Syu1 (yielding polyhydrated sulfate spectral signatures) and the LTYu (no spectral
536 signature detected); (ii) the clear sub-horizontal layering in Syu1 (foreground) compared to the
537 confusing situation in the LTYu (background) where, in most of the exposure, there are no clear layers
538 in the RMI mosaic.

539

540 Fig.2: Morphometric attributes of the Light-Toned Yardang unit from orbit. (A) Measurements of the
541 LTYu's attitudes. Length, width, aspect ratio, and direction of individual ridges form were measured
542 manually using *Adobe Illustrator*[®] software (metrics are provided in SM_Table 1). Colored bars
543 represent the ridge crest-lines. Insets are rose diagrams of measured crest-line directions. We restricted
544 our measurements to unmistakable yardang forms, the length of which is >30 m, due to a too possible
545 inaccurate measurement of the small features. (B, C, D, E) Distinctive morphological types of ridge
546 forms of the Middle, Upper, Top LTYu subunits respectively (B: HiRISE image ESP_030102_1750; C,
547 D: HiRISE image ESP_030880_1750; E: ESP_031803_1750). Dashed lines (C, D, E) highlight yardang
548 contours.

549

550 Fig. 3: Contact between the LTYu and the Syu1. (A) Geometric measurements of the unconformity that
551 bounds the overlying LTYu and the underlying Syu1. (B) Close-up of HiRISE image
552 ESP_028269_1750 (36.7 cm/pixel; 110 cm across resolved) showing that long axes of the yardang's
553 crest lines (dashed lines) of the upper Syu1 and lower LTYu are oriented differently. This provides
554 evidence that the Syu1 yardang forms developed prior to LTYu deposition indicating the unconformity

555 encompasses a long time interval. (C) Close-up of HiRISE image ESP_019698_1750 (29.1 cm/pixel;
556 87 cm across resolved) showing that now the partially-exhumed crater at the contact had been stripped
557 off and partially filled prior to the deposition of the LTYu.

558

559 Fig. 4: Orbital and ground views of the Lower LTY subunit. (A) HiRISE stereo terrain model showing
560 the texture detail of the yardang surface. Yardangs are elongated and transversally asymmetric forms.
561 The general stepped pattern results from the intersection of two linear trends (i.e. N67° and N83°). The
562 light-green, red and blue colored areas represent the ground projection (i.e., view shed) of the LD RMI
563 mosaic below. Cross-hatching indicates viewshed is outside of HiRISE stereo terrain model, and
564 therefore reduced to MOLA terrain model. (B) Mosaic of five LD RMI images (CCAM06251) taken
565 on sol 1183 at a distance of 6.9 km. The blue- and red-colored stripes are virtual projections transposed
566 onto HiRISE image A. N53° is the general strike direction of the slope. (C) LD RMI mosaic showing a
567 strike view of the beds (marked with red lines). The individual yardang forms are made up of evenly
568 distributed, subparallel and planar beds that dip away towards southeast (apparent dip of [4-12]°). The
569 general orientation of the yardang crests (black lines) is N67°, oblique to that of the slope.

570

571 Fig. 5: Close-up of CCAM06251 showing bedding geometries of the Lower LTYu. Most of the
572 observations in this area indicate a bedding orientation that dips away, with limited variation, in an
573 opposite direction to the local slope (i.e. southeast against northwest) so that bed strike sections actually
574 were traced. Bed traces (white lines) are extensive (i.e., several tens of meters long), and are mostly
575 planar and parallel. Only a few and minor local angular unconformities are traceable. Individual,
576 resistant yardang forms, which seem to be uniformly distributed down the general slope, show sets of
577 evenly stacked, thickening- and possibly steepening-upward beds.

578

579 Fig. 6: Lower LTY subunit. Mapped bed traces intersecting the land surface (red lines) over the HiRISE
580 stereo terrain model derived from full-resolution HiRISE images PSP_009149_1750 (27.7 cm/pixel; 83
581 cm across are resolved) paired with PSP_009294_1750. The light-green colored areas represent the
582 ground projection (i.e., view shed) of the LD RMI mosaic of Fig. 4A. The bed traces show a parallel,

583 linear to curvilinear pattern, suggesting planar geometry, with an apparent fairly uniform spacing. The
584 strike azimuth of the bed traces is quasi steady, and range between N31° and N55° directions (indicated
585 strike azimuths are general directions of local, bed trace clusters). The average dip is towards southeast
586 (i.e., N134°). Bedding planes are coincident with the local topography at some places. The dip
587 magnitude of these surfaces were not measurable because of their very limited extension. The dominant
588 wind direction is assumed reflective of the dominant direction of the sediment transport.

589

590 Fig. 7: Unscaled mechanical model that explains how the bed sets of the Lower LTY subunit were
591 deposited and preserved by winds dominantly blowing towards southeast, and then eroded by wind the
592 direction of which was approximately orthogonal to the dominant “depositional” wind.

593

594 Fig.8: Stratigraphic models for the Light-Toned Yardang unit. (A) Tentative stratigraphic cross section
595 of the LTYu, in context. The geometry of the major unconformity at the base of the LTYu suggests the
596 presence of an early moat around Mt Sharp, as predicted by Kite et al., 2016. The cross-section clearly
597 shows that the LTYu formed from climbing dunes on the side of a preexisting mound. Contact
598 geometries in between morphostratigraphic units of the LTYu are not certain, and there is no available
599 rover imaging from the surface perspective to constrain the stratal organization of the Middle to Top
600 LTY subunits (i.e., no LD RMI). In contrast to climbing bounding surfaces of the Lower LTY subunit,
601 internal bounding surfaces of the Middle to Top LTY subunits are difficult to discern at best (see
602 SM_Fig. 4) and drawn as subhorizontal, more gently dipping surfaces. (B) Tentative chronostratigraphic
603 chart (i.e., Wheeler Diagram) for the multistory deposition/erosion of the LTYu. Grey-shaded areas
604 express periods of deposition. Blank areas represent periods of non-deposition / erosion.

605 **References**

606

607 Anderson, R.B., Bell III, J.F., 2010. Geologic mapping and characterization of Gale Crater and
608 implications for its potential as a Mars Science Laboratory landing site. Mars J. 5, 76–128.
609 <http://dx.doi.org/10.1555/mars.2010.0004>.

610 Anderson, R.B., Edgar, L.A., Rubin, D.M., Lewis, K.W., Newman C., 2018. Complex bedding
611 geometry in the upper portion of Aeolis Mons, Gale crater, Mars. *Icarus* 314, 246-264.
612 <https://doi.org/10.1016/j.icarus.2018.06.009>

613 Blakey, R.C., Peterson, F., Kocurek, G., 1988. Synthesis of late Paleozoic and Mesozoic eolian deposits
614 of the Western Interior of the United States. *Sed. Geol.* 56, 3-127. [https://doi.org/10.1016/0037-](https://doi.org/10.1016/0037-0738(88)90050-4)
615 [0738\(88\)90050-4](https://doi.org/10.1016/0037-0738(88)90050-4).

616 Blakey, R.C., Jones, L.S., Havholm, K.G., 1996. Stratigraphic Analysis of Eolian Interactions with
617 Marine and Fluvial Deposits, Middle Jurassic Page Sandstone and Carmel Formation, Colorado Plateau,
618 U.S.A. *J. Sed. Res.* 66, 324-342. <https://doi.org/10.1306/D426833D-2B26-11D7-8648000102C1865D>.

619 Bridges, N.T., Banks, M.E., Beyer, R.A., Chuang, F.C, Noe Dobrea, E.Z., Herkenhoff, K.E., Keszthelyi,
620 L.P., Fishbaugh, K.E., McEwen, A.S., Michael, T.I., Thomson, B.J., Wray, J.J., 2010. Aeolian
621 bedforms, yardangs, and indurated surfaces in the Tharsis Montes as seen by the HiRISE camera:
622 evidence for dust aggregate. *Icarus* 205, 165-182. <http://dx.doi.org/10.1016/j.icarus.2009.05.017>.

623 Brookfield, M.E., 1992. Eolian systems, in: Walker, R.G., James, N.P. (Eds) *Facies Models: response*
624 *to sea level change*. *Geol. Ass. Canada, Memorial Univ. of Newfoundland*, pp.143-156.

625 Burr, D.M., Enga, M-T., Williams, R.M.E., Zimbelman, J.R., Howard, A.D., Brennand, T.A., 2009.
626 Pervasive aqueous paleoflow features in the Aeolis/Zephyria Plana region, Mars. *Icarus*, 200, 52–76.
627 <https://doi.org/10.1016/j.icarus.2008.10.014>.

628

629 **Chojnacki, M., Fenton, L.K., Weintraub, A.R., Edgar, L.A., Jodhpurkar, M.J., Edwards, M.S., 2020.**
630 **Ancient Martian Aeolian Sand Dune Deposits Recorded in the Stratigraphy of Valles Marineris and**
631 **Implications for Past Climates. *J. Geophys. Res.: Planets* 125, 9. <https://doi.org/10.1029/2020JE006510>.**

632

633 Di Pietro, I., Ori, G.G., Pondrelli, M., Francesco Salese, F., 2018. Geology of Aeolis Dorsa alluvial
634 sedimentary basin, Mars. *J. of Maps*, 14:2, 212-218. <https://doi.org/10.1080/17445647.2018.1454350>.

635

636 El-Baz, F., Breed, C.S., Grolier, M.J., McCauley, J.F. 1979. Eolian features in the western desert of
637 Egypt and some applications to Mars. *J. Geophys. Res.: Solid Earth* 84, 8205-8221.
638 <https://doi.org/10.1029/JB084iB14p08205>.
639

640 Fraeman, A.A., Ehlmann, B.L., Arvidson, R.E., Edwards, C.S., Grotzinger, J.P., Milliken, R.E., Quinn,
641 D.P., Rice, M.S., 2016. The stratigraphy and evolution of lower Mount Sharp from spectral,
642 morphological, and thermophysical orbital data sets. *J. Geophys. Res.: Planets* 121, 1713–1736.
643 <https://doi.org/10.1002/2016JE005095>.

644 Garvin, J.B., Sakimoto, S.E.H., Frawley, J.J., 2003. Craters on Mars: geometric properties from gridded
645 MOLA topography, Abstract 3277, in: *Proceedings of the Sixth International Conference on Mars*.
646 Pasadena, California. California Institute of Technology 20–25 July.

647 Grotzinger, J.P., Milliken, R.E., 2012. The Sedimentary Rock Record of Mars: Distribution, Origins,
648 and Global Stratigraphy, in: Grotzinger, J.P. & Milliken R.E. (Eds), *Sedimentary Geology of Mars*.
649 S.E.P.M. Spec. Publ. 12, pp. 1-48.

650 Grotzinger, J.P., Gupta, S., Malin, M.C., M.C., Rubin, D.M., Schieber, J., Siebach, K., Sumner, D.Y.,
651 Stack, K.M., Vasavada, A.R., Arvidson, R.E., Calef, F., Edgar, L., Fischer, W.F., Grant, J.A., Griffes,
652 J., Kah, L.C., Lamb, M.P., Lewis, K.W., Mangold, N., Minitti, M.E., Palucis, M., Rice, M., Williams,
653 R.M.E., Yingst, R.A., Blake, D., Blaney, D., Conrad, P., Crisp, J., Dietrich, W.E., Dromart, G., Edgett,
654 K.S., Ewing, R.C., Gellert, R., Hurowitz, J.A., Kocurek, G., Mahaffy, P., McBride, M.J., McLennan,
655 S.M., Mischna, M., Ming, D., Milliken, R., Newsom, H., Oehler, D., Parker, T.J., Vaniman, D., Wiens,
656 R.C., Wilson, S.A., 2015. Deposition, exhumation, and paleoclimate of an ancient lake deposit, Gale
657 crater, Mars. *Science* 350, aac7575. <http://dx.doi.org/10.1126/science.aac7575>.

658 Hartmann, W.K., 2005. Martian cratering 8: isochron refinement and the chronology of Mars.
659 *Icarus* 174, 294-320. <https://dx.doi.org/10.1016/j.icarus.2004.11.023>

660 Irmen, A.P., Vondra, C.F., 2000. Aeolian sediments in lower to middle Triassic rocks of central
661 Wyoming. *Sed. Geol.* 132, 69-88. [https://doi.org/10.1016/S0037-0738\(99\)00129-3](https://doi.org/10.1016/S0037-0738(99)00129-3).

662 Irwin, R.P., Howard, A.D., Craddock R.A., Moore, J.M. 2005. An intense terminal epoch of widespread
663 fluvial activity on early Mars: 2. Increased runoff and paleolake development, *J. Geophys. Res.* 110,
664 E12S15, doi:10.1029/2005JE002460.

665 Kirk, R.L., Howington-Kraus, E., Rosiek, M.R., Anderson, J.A., Archinal, B.A., Becker, K.J., Cook,
666 D.A., Galuszka, D.M., Geissler, P.E., Hare, T.M., Holmberg, I. M., Keszthelyi, L.P. Redding, B.L.
667 Delamere, W. A., Gallagher, D., Chapel, J.D., Eliason, E.M., King, R., McEwen, A.S., 2008. Ultrahigh
668 resolution topographic mapping of Mars with MRO HiRISE stereo images: Meter-scale slopes of
669 candidate Phoenix landing sites. *J. Geophys. Res.* 113, E12. <https://doi.org/10.1029/2007JE003000>.

670 Kite, E.S., Lewis, K.W., Lamb, M.P., Newman, C.E., Richardson, M.I. 2013. Growth and form of the
671 mound in Gale Crater, Mars: Slope wind enhanced erosion and transport. *Geology* 41, 543–546.
672 <https://doi.org/10.1130/g33909.1>.

673 Kite, E.S., Sneed, J., Mayer, D.P., Lewis, K.W., Michaels, T.I., Hore, A., Rafkin, S.C.R 2016. Evolution
674 of major sedimentary mounds on Mars: Buildup via anticompensational stacking modulated by climate
675 change. *J. Geophys. Res.: Planets* 121, 2282–2324. <https://doi.org/10.1002/2016JE005135>.

676

677 Kneissl, T., van Gasselt, S., Neukum, G. 2010. Measurement of strike and dip of geologic layers from
678 remote sensing data: New software tool for ArcGIS. *Lunar and Planetary Science Conference*, 41, 1640.

679 Kocurek, G. 1986. Origins of low-angle stratification in eolian deposits, in: Nickling, W.G. (Ed.), 16th
680 Annual Binghamton Geomorphology Symp. Allen and Unwin, London, pp. 177-193.

681 Kocurek, G., 1988. First-order and super bounding surfaces in eolian sequences – bounding surfaces
682 revisited. *Sed. Geol.* 56, 193-206. [https://doi.org/10.1016/0037-0738\(88\)90054-1](https://doi.org/10.1016/0037-0738(88)90054-1).

683 Laity, J.E., 2011. Wind erosion in drylands, in: Thomas, D.S.G. (Ed.), *Arid zone geomorphology:*
684 *Process, form and change in drylands* (3rd ed.). New York, NJ: John Wiley, pp. 539–568.

685 Laskar, J., Correia, A.C.M., Gastineau, M., Joutel, F., Levrard, B., 2004. Long term evolution and
686 chaotic diffusion of the insolation quantities of Mars. *Icarus* 170, 343–364.
687 <https://doi.org/10.1016/j.icarus.2004.04.005>.

688 Le Deit, L., Hauber, E., Fueten, F., Pondrelli, M., Rossi, A.P., Jaumann, R., 2013. Sequence of infilling
689 events in Gale Crater, Mars: Results from morphology, stratigraphy, and mineralogy. *J. Geophys. Res.:*
690 *Planets* 118, 2439–2473. <https://doi.org/10.1002/2012je004322>.

691 Le Mouélic, S., Gasnault, O., Herkenhoff, K.E., Bridges, N.T., Langevin, Y., Mangold, N., Maurice,
692 S., Wiens, R.C., Pinet, P., Newsom H.E., Deen R.G., Bell, J.F., Johnson, J.R., Rapin, W., Barraclough,
693 B., Blaney, D.L., Deflores, L., Maki, J., Malin, M.C., Pérez, R., Saccoccio, M., 2015. *The ChemCam*
694 *Remote Micro-Imager at Gale crater: Review of the first year of operations on Mars*. *Icarus* 249, 93-
695 107. <https://doi.org/10.1016/j.icarus.2014.05.030>.

696

697 Malin, M.C., Edgett K.S., 2000. Sedimentary Rocks of Early Mars. *Science* 290, 1927–1937.
698 <https://dx.doi.org/10.1126/science.290.5498.1927>.

699

700 Mandt, K.E., de Silva, S.L., Zimbelman, J.R., Crown, D.A., 2008. Origin of the Medusae Fossae
701 Formation, Mars: Insights from a synoptic approach. *J. Geophys. Res.* 113, E12011.
702 <https://doi.org/10.1029/2008JE003076>.

703

704 Mandt, K.E., de Silva, S.L., Zimbelman, J.R., Wyrick, D., 2009. Distinct erosional progressions in the
705 Medusae Fossae formation, Mars, indicate contrasting environmental conditions. *Icarus* 204, 471–477.
706 <https://doi.org/10.1016/j.icarus.2009.06.031>.

707 Marzolf, J.E., 1988. Controls on late Paleozoic and early Mesozoic eolian deposition of the western
708 United States. *Sed. Geol.* 56, 167-191. [https://doi.org/10.1016/0037-0738\(88\)90053-X](https://doi.org/10.1016/0037-0738(88)90053-X).

709 McCauley, J.F., 1973. Mariner 9 evidence for wind erosion in the equatorial and mid-latitude regions of
710 Mars. *J. Geophys. Res.* 78, 4123-4137. <https://doi.org/10.1029/JB078i020p04123>.

711 McCauley, J.F., Grolier, M.J., Breed C.S., 1977. Yardangs, in Doehring, D.O. (Ed.), *Geomorphology in*
712 *Arid Regions*. Allen and Unwin, Boston (USA), pp. 233–269.

713 Milliken R.E, Grotzinger, J.P., Thomson, B.J., 2010. Paleoclimate of Mars as captured by the
714 stratigraphic record in Gale Crater. *Geophys. Res. Lett.* 37, L04201.
715 <https://doi.org/10.1029/2009GL041870>.

716

717 Neukum, G., Ivanov B.A., Hartmann W.K., 2001. Cratering records in the inner solar system in relation
718 to the lunar reference system *Space Sci. Rev.* 96, 1-4, 55-86. <https://doi:10.1023/A:1011989004263>.

719

720 Peret L., Gasnault O., Dingler R., Langevin Y., Bender S., Blaney D., Clegg S., Clewans C., Delapp D.,
721 Donny C., Johnstone S., Little C., Lorigny E., McInroy R., Maurice S., Mittal N., Pavri B., Perez R.,
722 Wiens R.C., and Yana C., 2016. Restoration of the autofocus capability of the ChemCam instrument
723 onboard the Curiosity rover. *SpaceOps 2016 Conference*, (AIAA 2016-2539). [https://](https://doi:10.2514/6.2016-2539)
724 doi:10.2514/6.2016-2539.

725

726 Quantin-Nataf, C., Craddock, R.A., Dubuffet, F., Lozac'h, L., Martinot, M., 2019. Decline of crater
727 obliteration rates during early martian history. *Icarus* 317, 427-433.
728 <https://doi.org/10.1016/j.icarus.2018.08.005>.

729

730 Rossi, A.P., Neukum, G., Pondrelli, M., van Gasselt, S., Zegers, T., Hauber, E., Chicarro, A., Foing, B.,
731 2008. Large spring deposits on Mars? *J. Geophys. Res.: Planets* 113, E08016.
732 <https://doi.org/10.1029/2007JE003062>.

733

734 Scott, D.H., Chapman, M.G. 1995. Geologic and topographic maps of the Elysium Paleolake basin,
735 Mars. *U.S. Geol. Surv. Misc. Invest. Ser.*, MAP I-2397.

736 Tanaka, K.L., Skinner, J.A., Jr., Dohm, J.M., Irwin, R.P., III, Kolb, E.J., Fortezzo, C.M., Platz, T.,
737 Michael, G.G., Hare, T.M., 2014. Geologic map of Mars: U.S. Geological Survey Scientific
738 Investigations Map 3292, scale 1:20,000,000, pamphlet 43 p. <https://dx.doi.org/10.3133/sim3292>.

739 Tewes, D.W., Loope, D.B., 1992. Palaeo- yardangs: wind-scoured desert landforms at the Permo-
740 Triassic unconformity. *Sedimentology* 39, 251-261. [https://doi.org/10.1111/j.1365-
741 3091.1992.tb01037.x](https://doi.org/10.1111/j.1365-3091.1992.tb01037.x).

742 Thomson, B.J., Bridges, N.T., Milliken, R.E., Baldrige, A., Hook, S.J., Crowley, J.K., Marion, G.M.,
743 de Souza Filho, C.R., Brown, A.J., Weitz, C.M. 2011. Constraints on the origin and evolution of the
744 layered mound in Gale Crater, Mars using Mars Reconnaissance Orbiter data. *Icarus* 214, 413–432.
745 <https://doi.org/10.1016/j.icarus.2011.05.002>

746 Vasavada, A.R., Grotzinger, J.P., Arvidson, R.E., Calef, F. J., Crisp, J. A., Gupta, S., Hurowitz, J.A.,
747 Mangold N., Maurice, S., Schmidt, M.E., Wiens, R.C. Williams, R.M.E., Yingst, R.A., 2014. Over view
748 of the Mars Science Laboratory mission: Bradbury Landing to Yellowknife Bay and beyond. *J.*
749 *Geophys. Res.* 19, 1134–1161. <https://doi:10.1002/2014JE004622>.

750 Ward, A.W., 1979. Yardangs on Mars: Evidence of recent wind erosion. *J. Geophys. Res.* 84, 8147-
751 8167. <https://doi.org/10.1029/JB084iB14p08147>.

752 Wang, J., Xiao, L., Reiss, D., Hiesinger, H., Huang, J., Xu, Y., Zhao, J., Xiao, Z., Komatsu, G., 2008.
753 Geological Features and Evolution of Yardangs in the Qaidam Basin, Tibetan Plateau (NW China): A
754 Terrestrial Analogue for Mars. *J. Geophys. Res.: Planets* 123, 2336–2364.
755 <https://doi.org/10.1029/2018JE005719>.

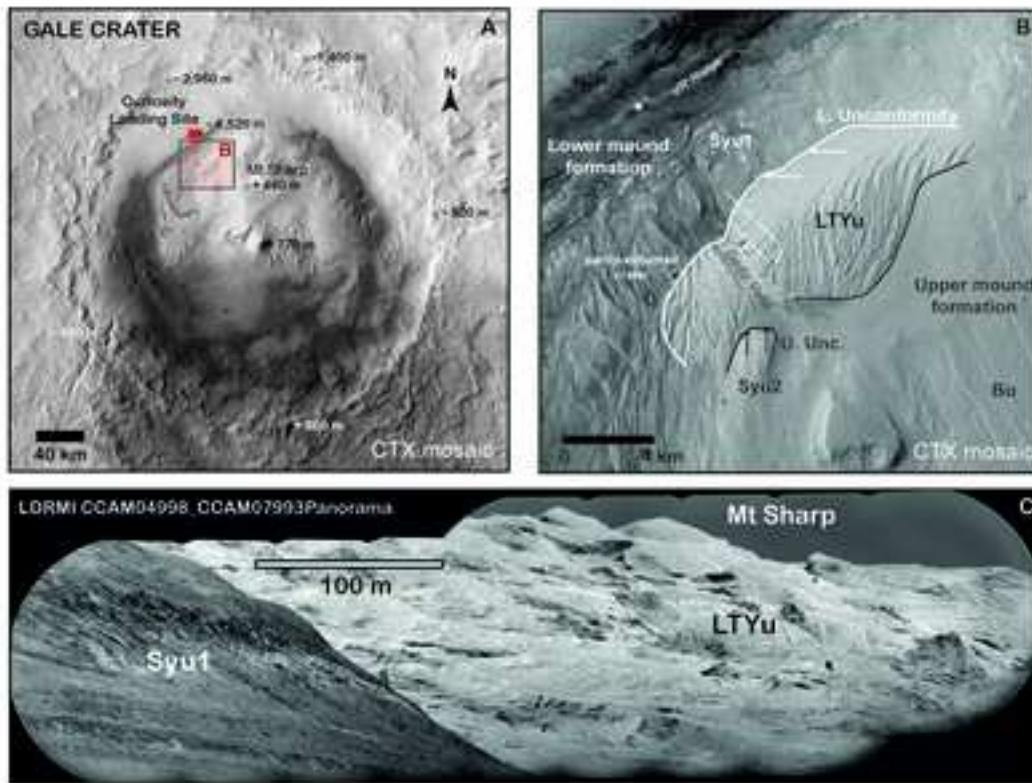
756 Wells, G.L., Zimbelman, J.R., 1989. Extraterrestrial arid surface processes, in: Thomas, D.S.G. (Ed.),
757 *Arid Zone Geomorphology*. Belhaven, London, pp. 335–358.

758 Wilson, I.G., 1971. Desert sandflow basins and a model for the origin of ergs. *The Geogr. J.* 137, 180-
759 199. <https://doi.org/10.2307/1796738>.

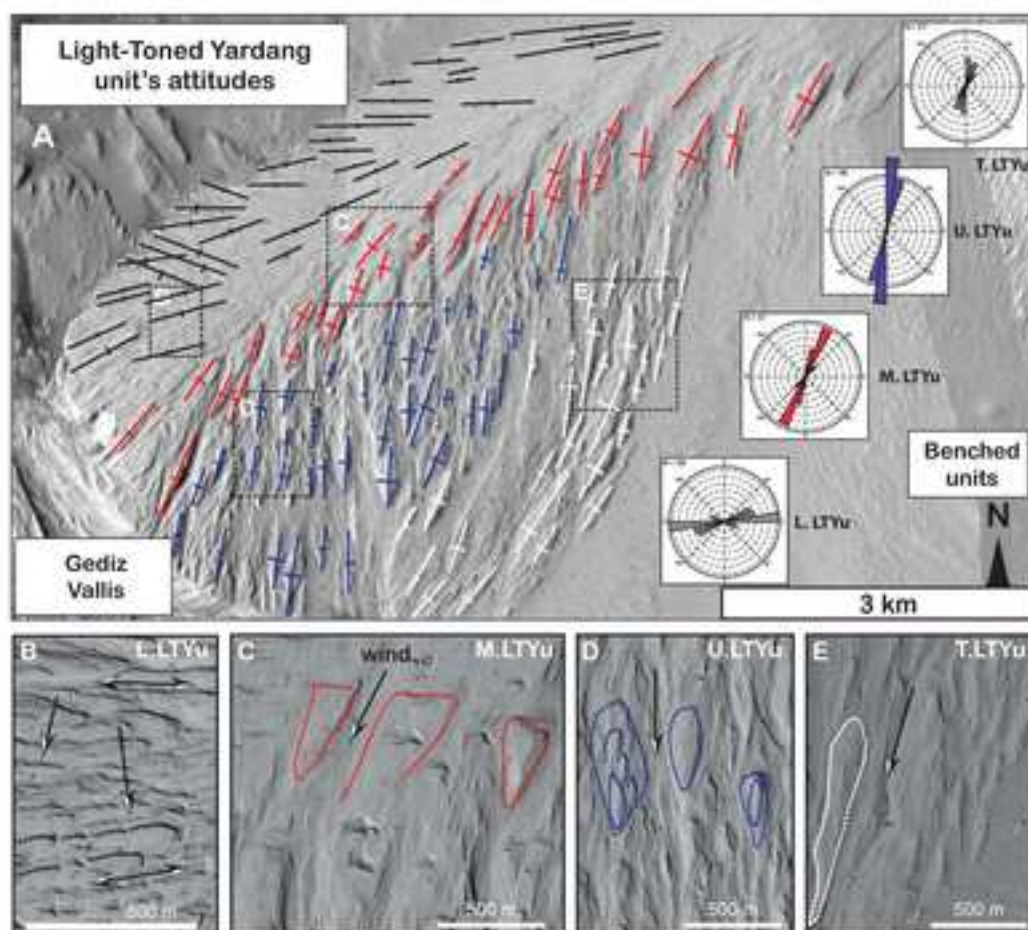
760 Zhao, N.C., Chenb, J., Hu, C., 2018. Automatic extraction of yardangs using Landsat 8 and UAV
761 images: A case study in the Qaidam Basin, China. *Aeolian Research* 33, 53-51.
762 <https://doi.org/10.1016/j.aeolia.2018.05.002>.

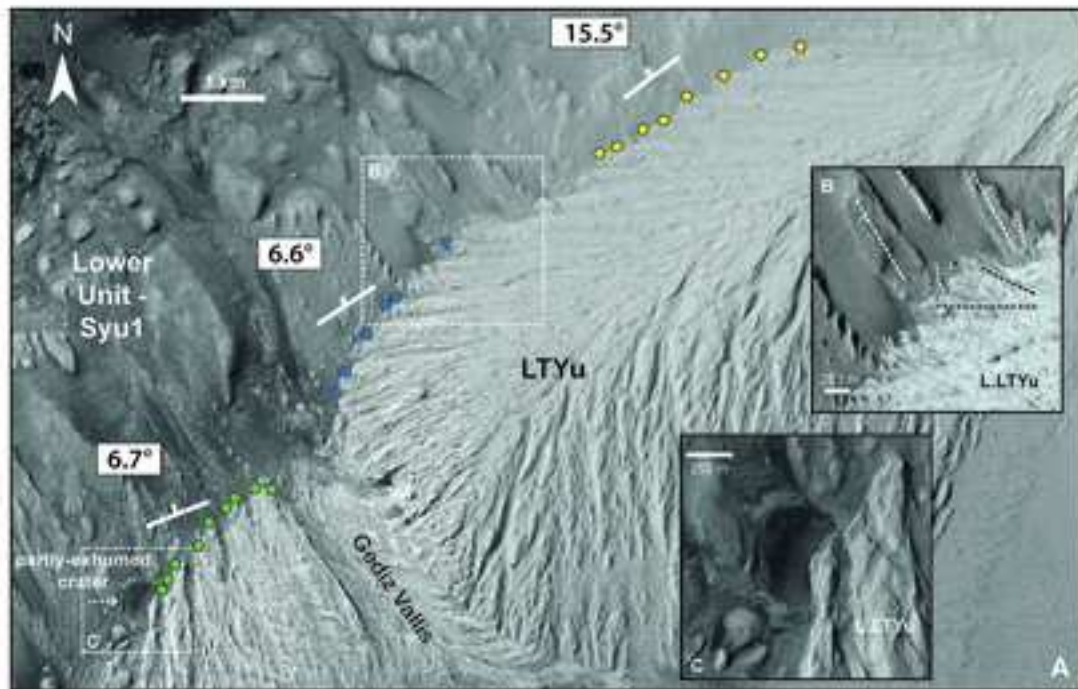
763 Zimbelman, J.R., Griffin, L.J., 2010. HiRISE images of yardangs and sinuous ridges in the lower
764 member of the Medusae Fossae Formation, Mars. *Icarus* 205, 198–210.
765 <https://doi.org/10.1016/j.icarus.2009.04.003>.

766 Zimbelman, J.R., Scheidt, S.P., 2012. Hesperian age for Western Medusae Fossae Formation, Mars.
767 *Science* 336 (6089), 1683. <http://dx.doi.org/10.1126/science.1221094>.

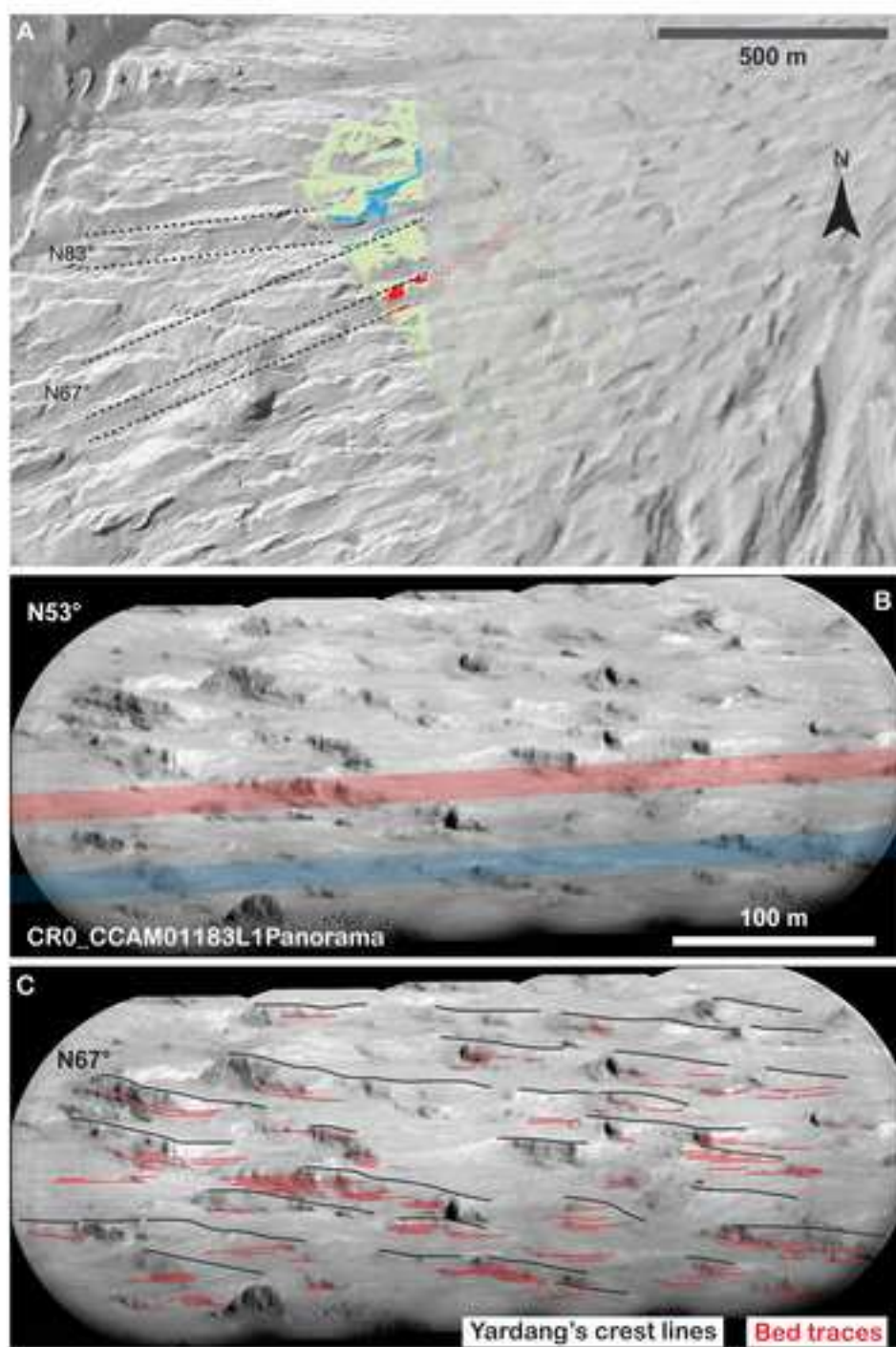


Dromart et al. Fig. 1

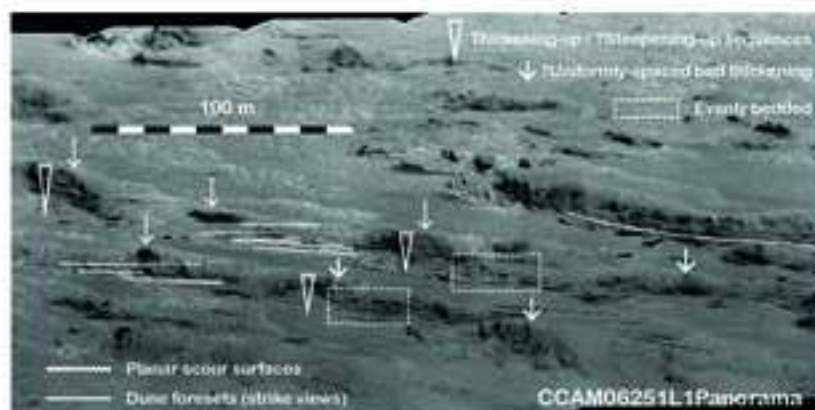




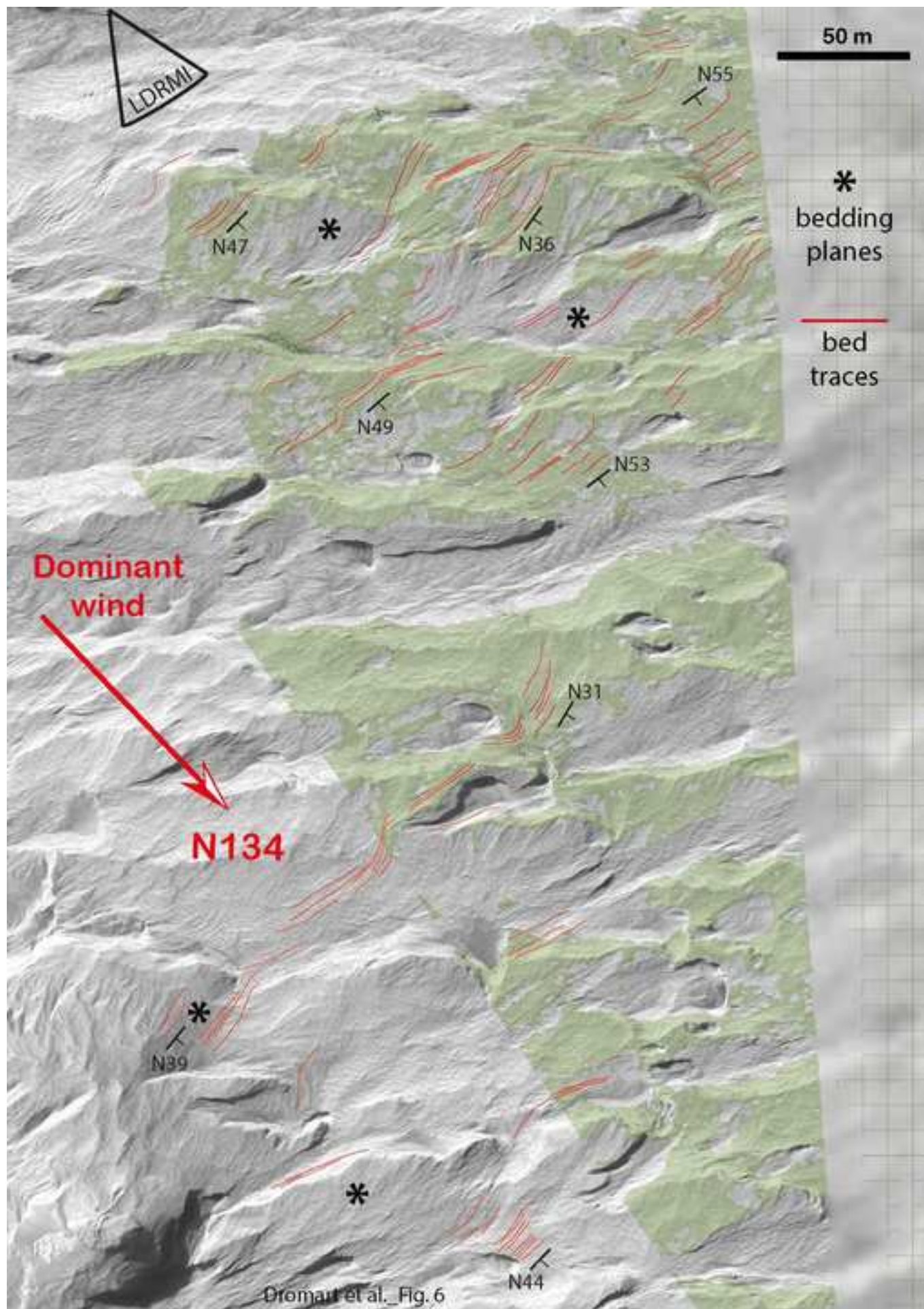
Dromart et al._Fig. 3

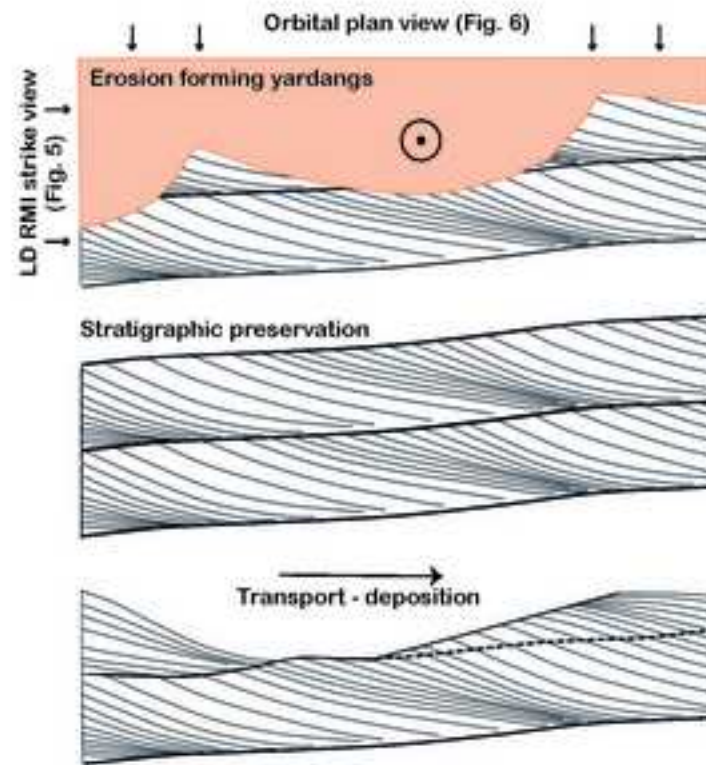


Dromart et al. Fig. 4

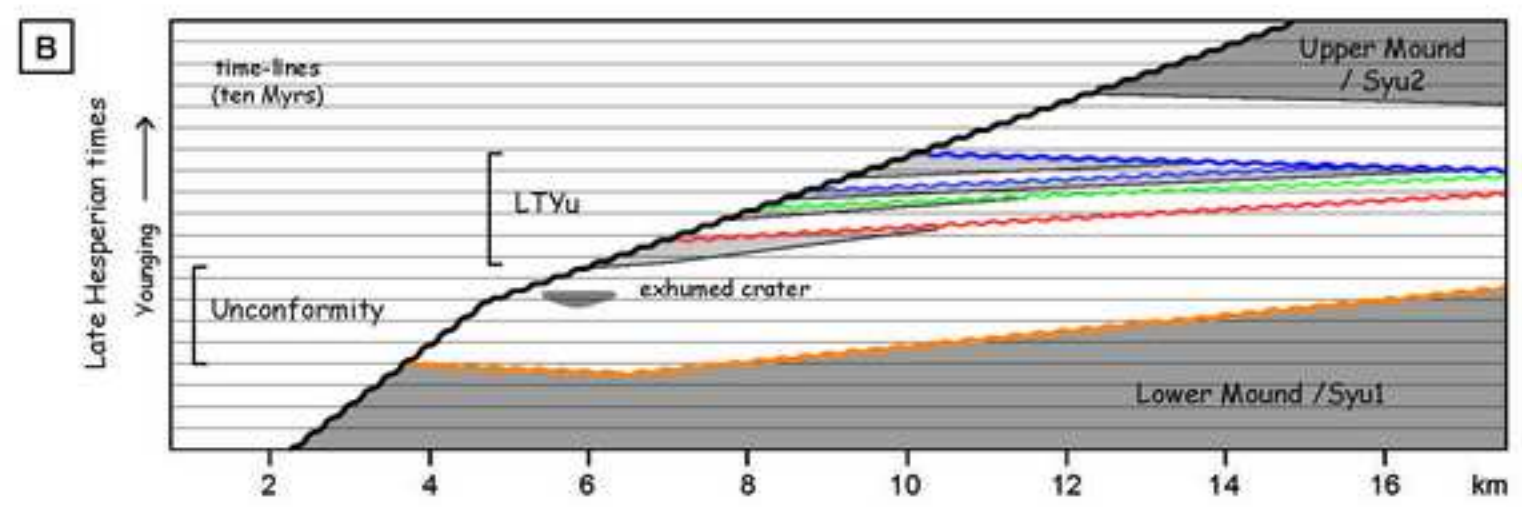
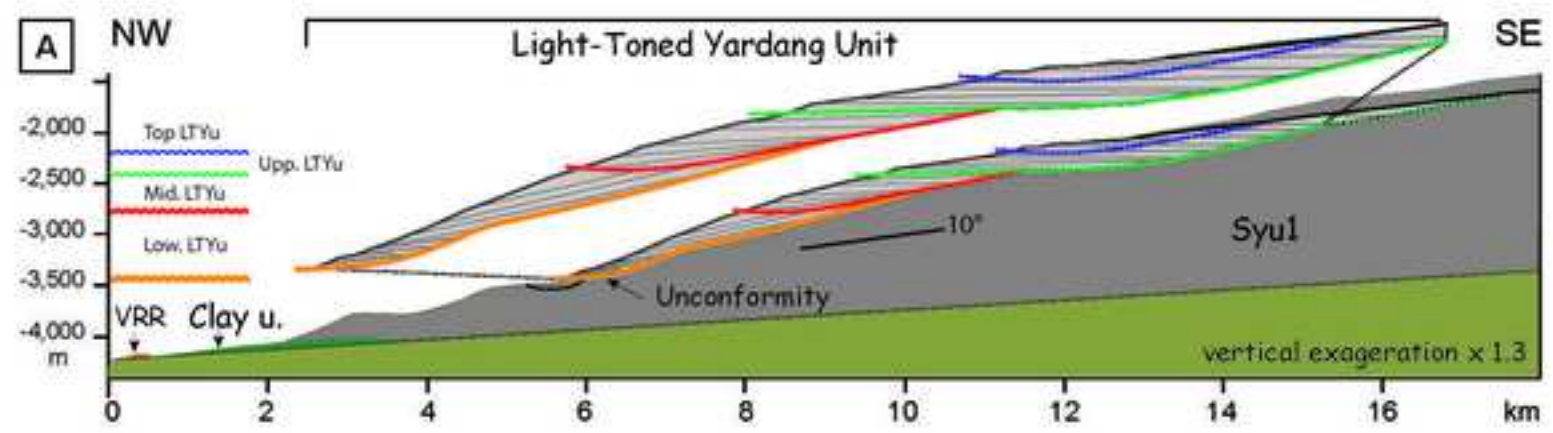


Dromart et al._Fig. 5

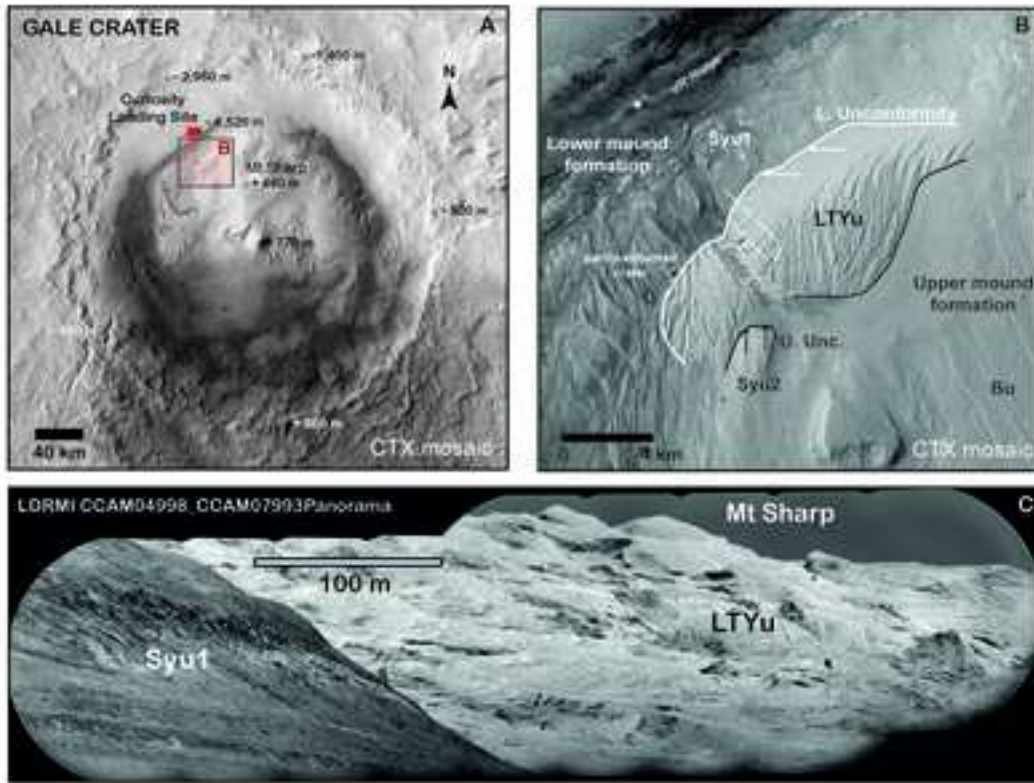




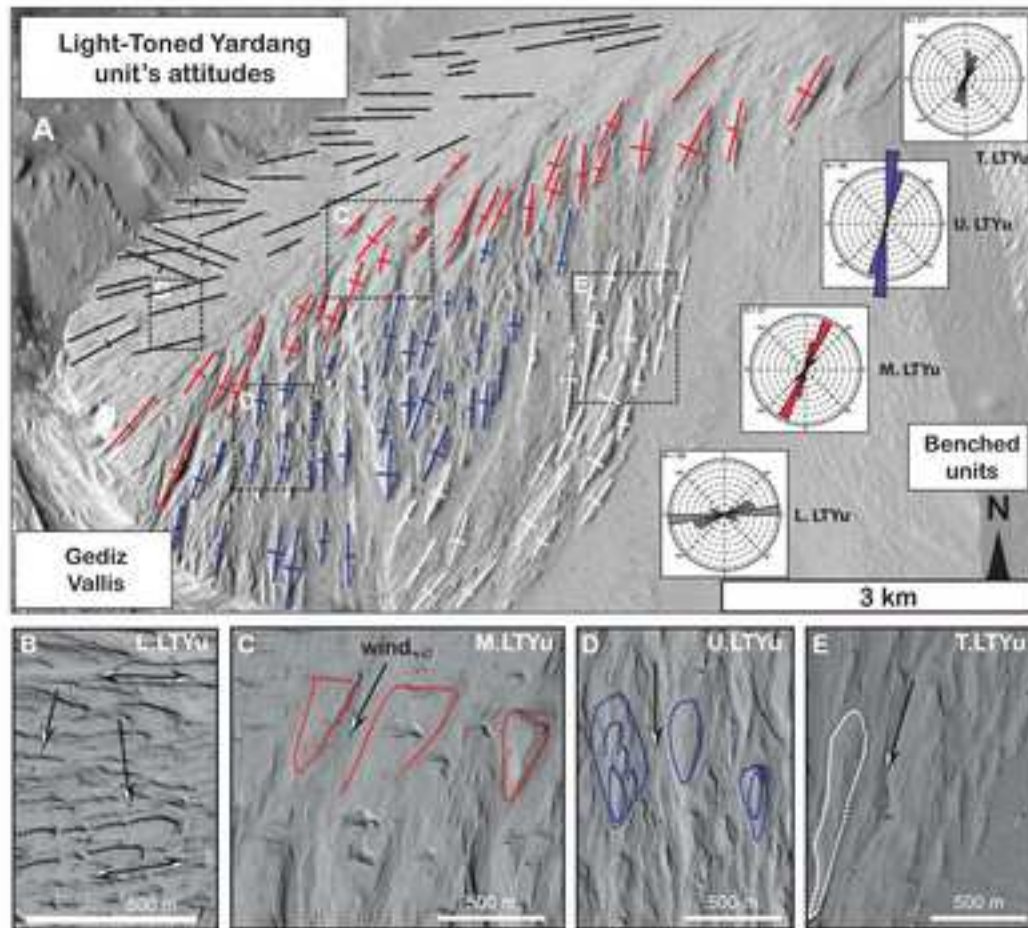
Dromart et al._Fig. 7



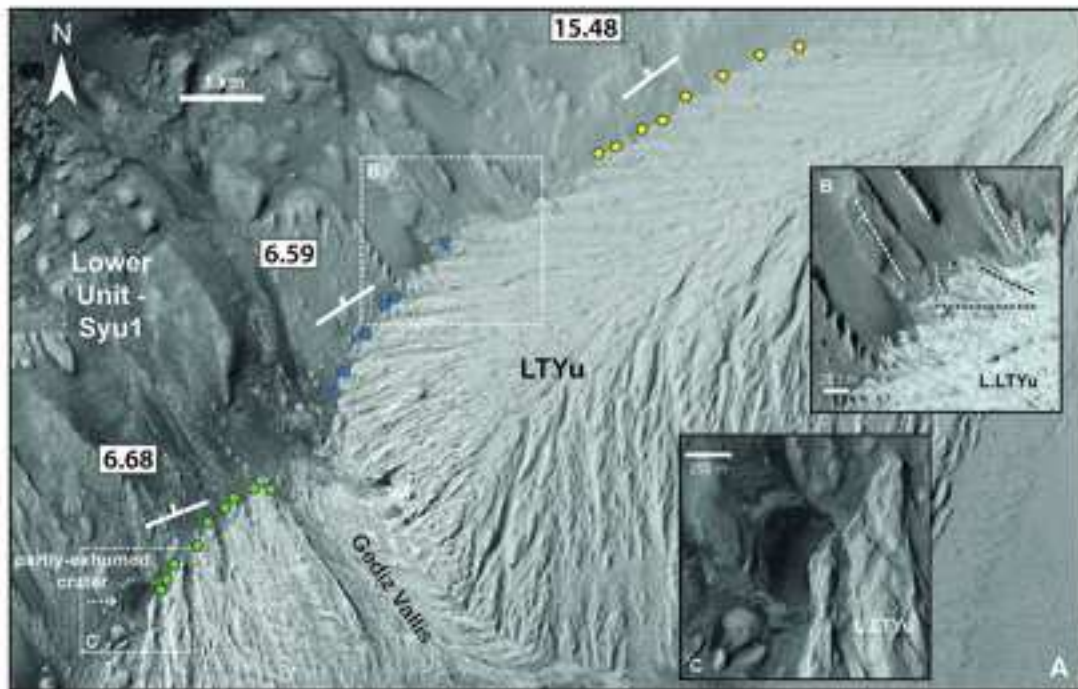
Dromart et al._Fig. 8



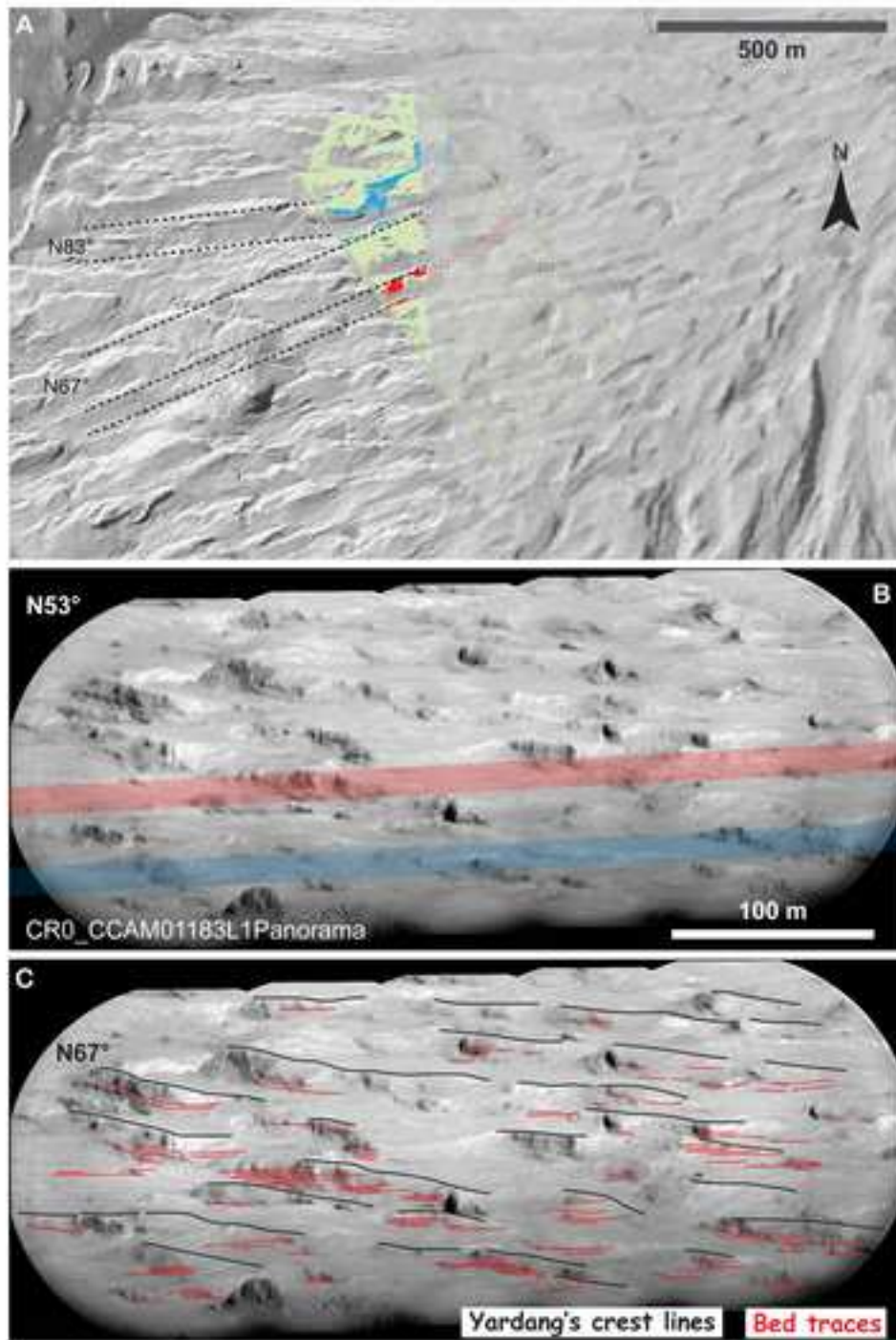
Dromart et al. Fig. 1



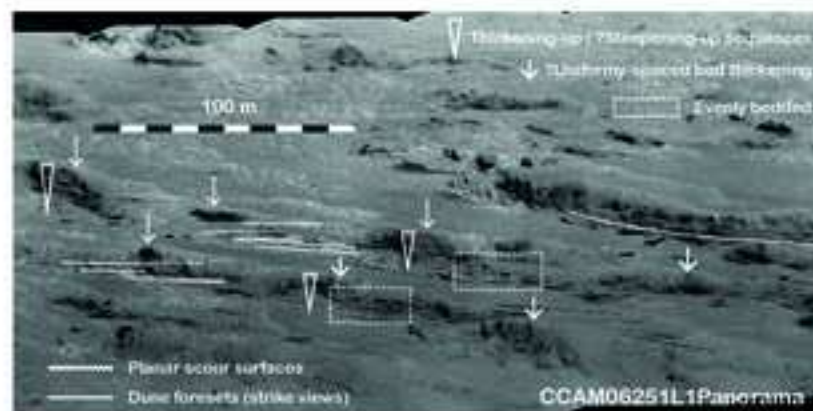
Dromart et al., Fig. 2



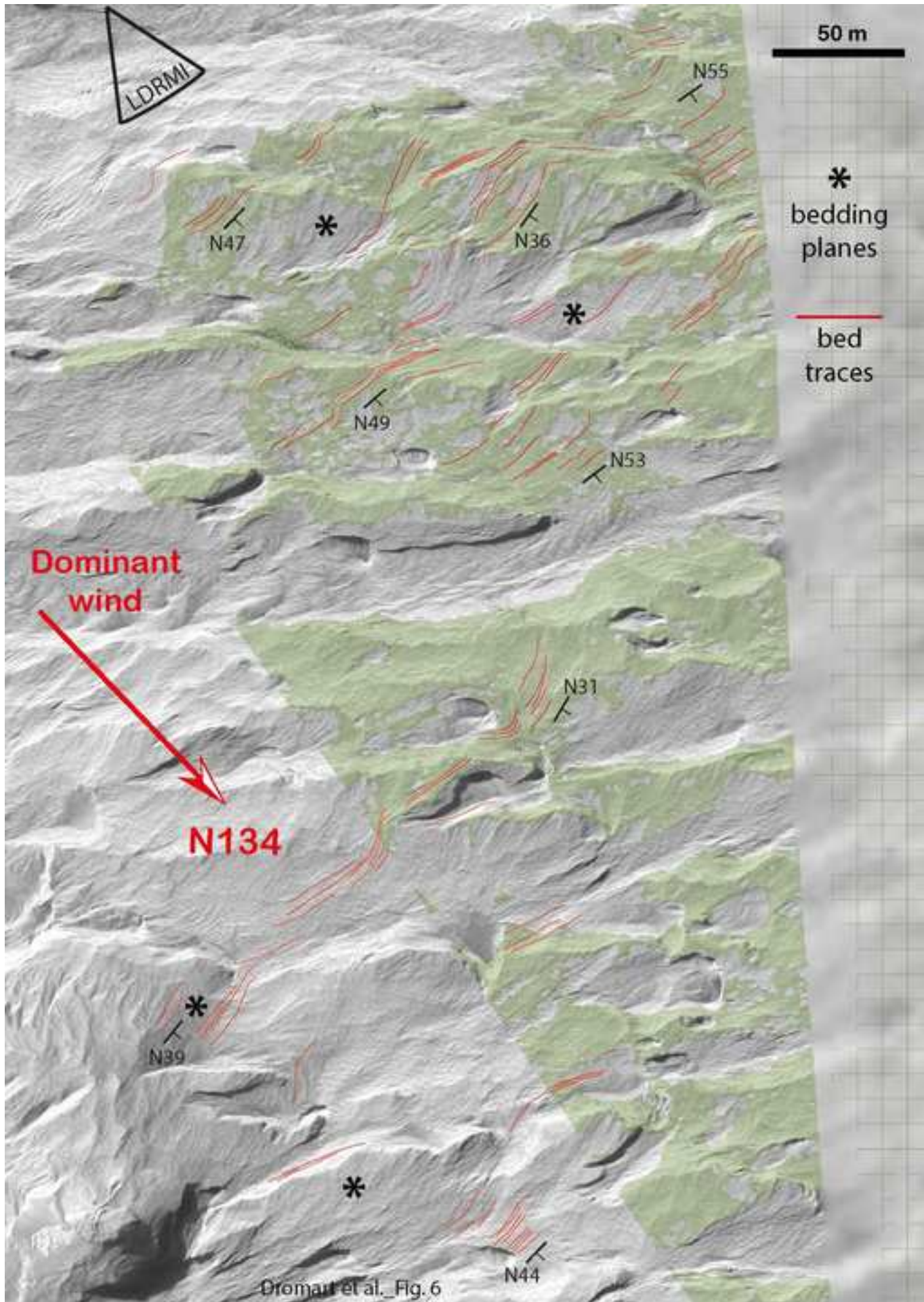
Dromart et al._Fig. 3



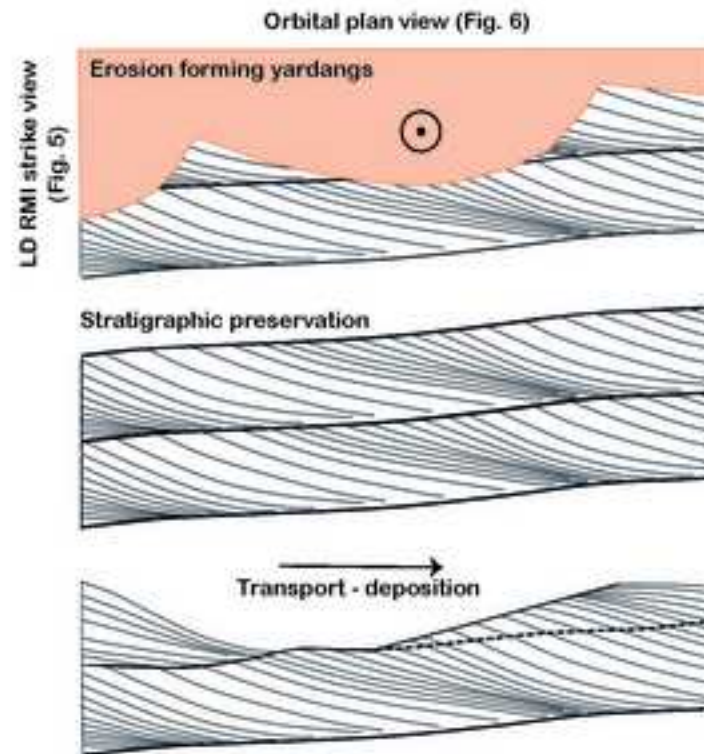
Dromart et al. Fig. 4



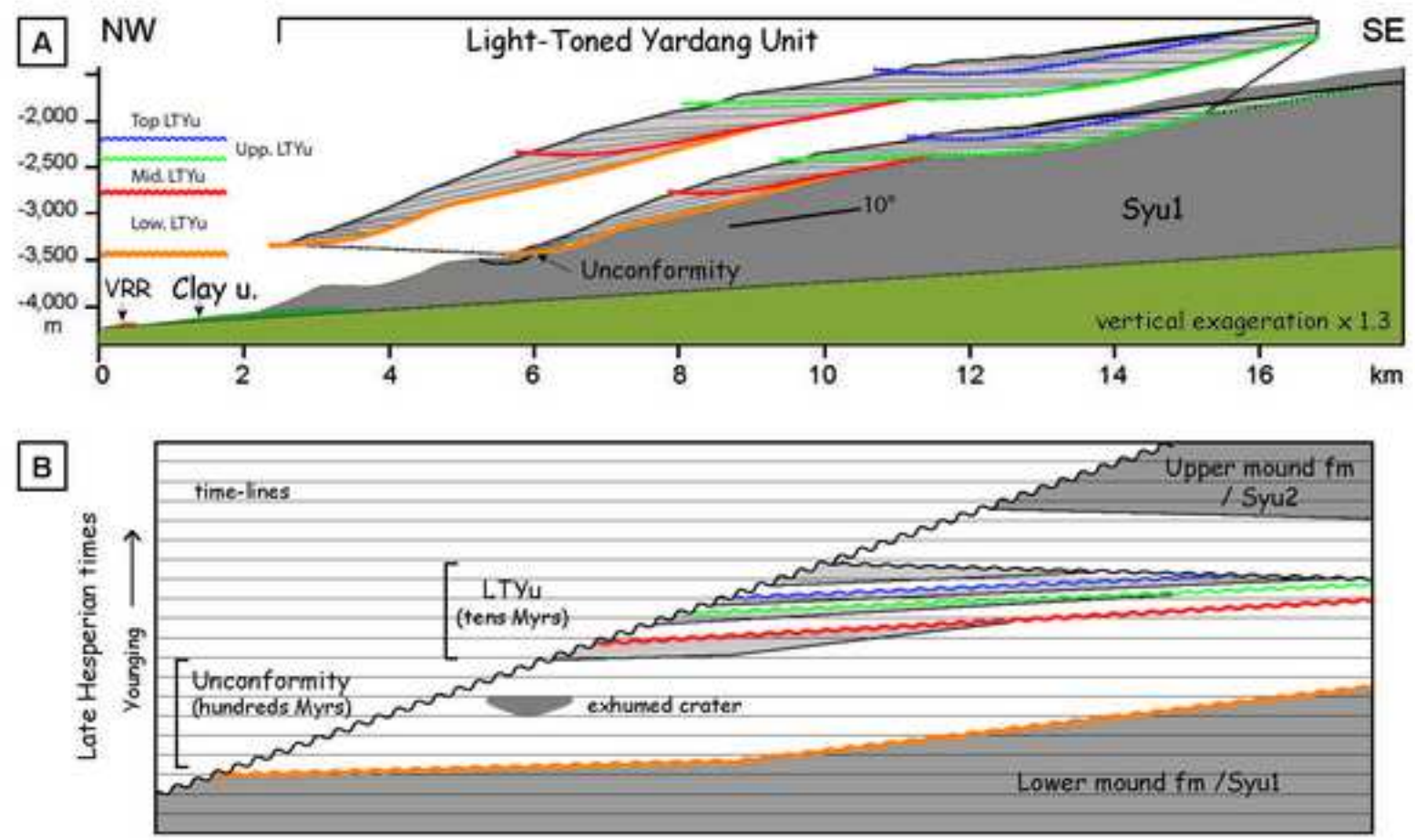
Dromart et al._Fig. 5



Dromart et al. Fig. 6



Dromart et al._Fig. 7

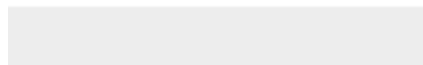


Dromart et al., Fig. 8



[Click here to access/download](#)

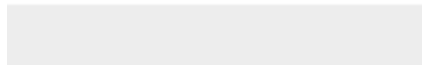
Supplementary material for online publication only
SM_Text 1.pdf

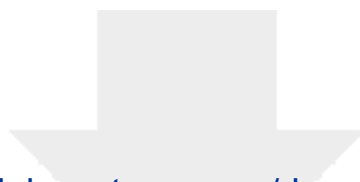




[Click here to access/download](#)

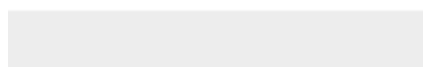
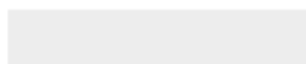
Supplementary material for online publication only
SM_Fig 1.jpg

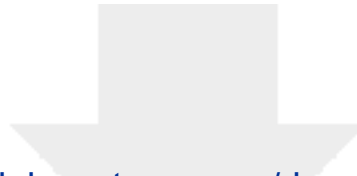




[Click here to access/download](#)

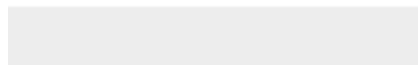
Supplementary material for online publication only
SM_Fig 2.jpg





[Click here to access/download](#)

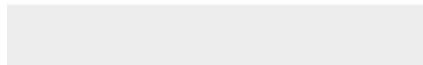
Supplementary material for online publication only
SM_Fig 3.jpg





[Click here to access/download](#)

Supplementary material for online publication only
SM_Table 1.pdf



Declaration of interests

The authors declare that they have no known competing financial interests or personal relationships that could have appeared to influence the work reported in this paper.

The authors declare the following financial interests/personal relationships which may be considered as potential competing interests:

Author contributions

G.D. analyzed the image data, conceived and drafted the figures, conceived and wrote the manuscript. L.L. quantified the geometry of the LTYu basal bounding surface. W.R. projected the LD RMI mosaics as view sheds onto the DTMs. O.G. and SL carried out corrections of LD RMI mosaics. C. Q. calculated the lapse-time required for a surface to have a significant chance of having been impacted. N.M., D.R., J.L., S.M., H.N., P.P., L.S., R.W. contributed to the interpretation of the data and revisions of the manuscript.